

Insights on the X–ray weak quasar phenomenon from *XMM–Newton* monitoring of PHL 1092

G. Miniutti,^{1*} W. N. Brandt,^{2,3} D. P. Schneider,^{2,3} A. C. Fabian,⁴ L. C. Gallo,⁵ and Th. Boller⁶

¹*Centro de Astrobiología (CSIC–INTA), Dep. de Astrofísica; ESA, P.O: Box 78, E-28691, Villanueva de la Cañada, Madrid, Spain*

²*Department of Astronomy and Astrophysics, The Pennsylvania State University, 525 Davey Lab., University Park, PA 16802, USA*

³*Institute for Gravitation and the Cosmos, The Pennsylvania State University, University Park, PA 16802, USA*

⁴*Institute of Astronomy, Madingley Road, Cambridge CB3 0HA*

⁵*Department of Astronomy & Physics, Saint Mary's University, 923 Robie Street, Halifax, NS B3H 3C3*

⁶*Max–Planck–Institut für extraterrestrische Physik, Postfach 1312, 85741 Garching, Germany*

6 November 2018

ABSTRACT

PHL 1092 is a $z \sim 0.4$ high–luminosity counterpart of the class of Narrow–Line Seyfert 1 galaxies. In 2008, PHL 1092 was found to be in a remarkably low X–ray flux state during an *XMM–Newton* observation. Its 2 keV flux density had dropped by a factor of ~ 260 with respect to a previous observation performed 4.5 yr earlier. The UV flux remained almost constant, resulting in a significant steepening of the optical–to–X–ray slope α_{ox} from -1.57 to -2.51 , making PHL 1092 one of the most extreme X–ray weak quasars with no observed broad absorption lines (BALs) in the UV. We have monitored the source since 2008 with three further *XMM–Newton* observations, producing a simultaneous UV and X–ray database spanning almost 10 yr in total in the activity of the source. Our monitoring program demonstrates that the α_{ox} variability in PHL 1092 is entirely driven by long–term X–ray flux changes. We apply a series of physically–motivated models with the goal of explaining the UV–to–X–ray spectral energy distribution (SED) and the extreme X–ray and α_{ox} variability. We consider three possible models: i) A *breathing corona* scenario in which the size of the X–ray emitting corona is correlated with the X–ray flux. In this case, the lowest X–ray flux states of PHL 1092 are associated with an almost complete collapse of the X–ray corona down to the marginal stable orbit; ii) An absorption scenario in which the X–ray flux variability is entirely due to intervening absorption. If so, PHL 1092 is a quasar with standard X–ray output for its optical luminosity, appearing as X–ray weak at times due to absorption; iii) A disc–reflection–dominated scenario in which the X–ray emitting corona is confined within a few gravitational radii from the black hole at all times. In this case, the intrinsic variability of PHL 1092 only needs to be a factor of ~ 10 rather than the observed factor of ~ 260 . We discuss these scenarios in the context of non–BAL X–ray weak quasars.

Key words: galaxies: active – quasars: individual: PHL 1092 – X-rays: galaxies – X-rays: individual: PHL 1092

1 INTRODUCTION

X–ray emission is a universal property of efficiently accreting black holes (BH) and its origin is, most likely, Compton up–scattering of the UV/EUV disc emission in an X–ray corona of hot electrons (e.g. Haardt, Maraschi & Ghisellini 1994). There are, however, a few examples of Active Galactic Nuclei (AGN) where the corona appears to emit X–rays much less efficiently than usual, with an X–ray output ~ 10 – 100 times lower than that expected based upon the optical/UV emission properties. These are known as X–ray weak

AGN which often exhibit broad absorption lines (BALs) in the UV, suggesting an absorption–driven interpretation of their X–ray weakness (Brandt, Laor & Wills 2000). Indeed, X–ray absorption has been convincingly detected in a number of BAL quasars (e.g. Brinkmann et al. 1999; Wang et al. 1999; Gallagher et al. 2001, 2004; Mathur et al. 2001; Chartas et al. 2002, 2007, 2009).

However, a growing number of X–ray weak quasars do not show any detectable BALs in their UV spectra (e.g. Wu et al. 2011). The best–studied case is that of PHL 1811 (Leighly et al. 2001, 2007a, 2007b). This quasar has been observed several times in X–rays and is persistently X–ray weak. Its X–ray spectrum shows no sign of absorption of a higher level X–ray flux, so that PHL 1811

* E-mail: gminiutti@cab.inta-csic.es

appears to be intrinsically X-ray weak. The C IV emission line is weak, blueshifted and asymmetric, indicating the presence of a wind. The near-UV spectrum is dominated by Fe II and Fe III emission-line blends and unusually low-ionisation lines. Leighly et al. (2007b) demonstrated, using detailed photo-ionisation modelling, that the optical/UV emission lines are consistent with a wind plus disc scenario in which C IV is produced in the outflow while the low-ionisation lines (e.g. Mg II) are associated with the denser disc at larger radii and see an ionising continuum filtered through the wind itself. Indeed, a soft, X-ray weak ionising continuum can explain the unusual optical/UV line properties if filtering through the wind is considered for the disc-lines. The question in PHL 1811 and similar sources is then whether the X-ray emission is intrinsically weak or due to intervening X-ray-only absorption.

Here we consider the case of PHL 1092 which recently became one of the most extreme X-ray weak non-BAL quasars known (see below). PHL 1092 ($z = 0.396$) is a radio-quiet quasar with outstanding Fe II emission (Bergeron & Kunth 1980, 1984; Kwan et al 1995). Its broad line widths of $\sim 1800 \text{ km s}^{-1}$ and a ratio $[\text{O III}]\lambda 5007 / \text{H}\beta \sim 0.9$, together with the strong Fe II emission ($\text{Fe II}/\text{H}\beta = 1.81$), classify PHL 1092 as a high-luminosity Narrow-Line Seyfert 1 (NLS1) galaxy (Osterbrock & Pogge 1985). The bolometric luminosity of PHL 1092 is $4 - 5 \times 10^{46} \text{ erg s}^{-1}$. Its UV spectrum shows relatively weak, broad, and blueshifted C IV emission and presents many analogies with the prototypical non-BAL X-ray weak quasar PHL 1811 (Wu et al. 2011).

In 2008, PHL 1092 was found to be in a remarkably low X-ray flux state during an *XMM-Newton* observation with a 2 keV flux-density drop of ~ 260 with respect to a previous 2003 *XMM-Newton* exposure (Miniutti et al. 2009b). The UV flux remained almost constant, resulting in a significant steepening of the optical-to-X-ray slope α_{ox} from -1.57 to -2.51 and showing that even extreme X-ray weakness can in fact be a transient phenomenon. Quasi-simultaneous optical spectra from Mg II to H β did not reveal significant changes with respect to historical ones allowing us to exclude the presence of a Mg II BAL.

In order to shed light on the X-ray weakness phenomenon in non-BAL quasars, we have monitored PHL 1092, obtaining three observations with *XMM-Newton* since 2008, and another optical spectrum which is quasi-simultaneous with our last X-ray pointing in 2010. We report here results from our monitoring campaign spanning almost 10 yr in total in the activity of the source. Our observations provide simultaneous UV and X-ray data with which we follow the long-term X-ray and optical/UV variability of this remarkable source. We consider a series of physically motivated models that can reproduce the UV-to-X-ray data at the different probed X-ray flux levels, and we discuss the implications of our results in the context of non-BAL X-ray weak quasars.

2 OBSERVATIONS

PHL 1092 was observed with *XMM-Newton* on 6 occasions. The first observation was performed on 2000 July 31, but due to problems with the European Photon Imaging Camera (EPIC) cameras (Strüder et al. 2001; Turner et al. 2001), only X-ray and UV light curves could be obtained. The source was re-observed three years later, resulting in a complete set of ODF files for all detectors. Results from both observations were reported by Gallo et al. (2004). We obtained a further ~ 60 ks observation on 2008 January 20 which caught the source in an extreme X-ray weak state with a soft X-ray flux drop of ~ 260 with respect to the 2003 observation

as discussed by Miniutti et al. (2009b). The source was monitored during the two subsequent years, with three *XMM-Newton* observations performed on 2009 June 27, 2010 July 7, and 2010 December 30. The 2008 observation was complemented with quasi-simultaneous optical spectra at the Hobby-Eberly and William Herschel Telescopes on January 30 and February 14 respectively, and an additional optical spectrum was obtained at the Hobby-Eberly Telescope on 2010 October 31. The HET data cover the $\approx 4300\text{--}7300 \text{ \AA}$ spectral range, while the WHT spectrum is obtained in the $\approx 3600\text{--}5180 \text{ \AA}$ and $\approx 5950\text{--}9090 \text{ \AA}$ range.

The observation log of the *XMM-Newton* observations is given in Table 1. The *XMM-Newton* ODF files were processed using the dedicated Science Analysis Software (SAS v11.0) to obtain calibrated event lists which were filtered for bad pixels and high background flaring. Single and double events were selected to extract scientific products for the EPIC detectors. We optimised the spectral extraction areas of the source to maximise the signal-to-noise ratio resulting in observation-dependent circular extraction regions of radii in the range of $25''\text{--}40''$. Background spectra were extracted from larger off-source areas. Here we make use of the EPIC-pn data from all observations because of its higher sensitivity with respect to the MOS detectors. However, we have checked that the spectra obtained from the pn and MOS detectors are consistent with each other, which is indeed the case. All pn spectra were grouped to produce a minimum of 25 counts per energy channel. We also report results from the *XMM-Newton* Optical Monitor (OM), which was used to derive the monochromatic fluxes in the different available filters in each observation. The OM generally takes multiple images per filter. As the intra-observation variability was found to be marginal at best, the fluxes reported in Table 1 are obtained from the average count rate in each observation and filter using the conversion factors between OM count rate and monochromatic flux reported in the *XMM-Newton* SAS user guide.¹ Throughout this paper, we adopt a cosmology with $H_0 = 70 \text{ km s}^{-1} \text{ Mpc}^{-1}$, $\Omega_\Lambda = 0.73$, and $\Omega_M = 0.27$.

3 DRAMATIC LONG-TERM X-RAY VARIABILITY

The historical soft X-ray flux light curve of PHL 1092 is shown in Fig. 1. As can be seen, PHL 1092 was observed in an extremely low flux state in 2008, which was reported and discussed by Miniutti et al. (2009b). Its soft X-ray flux then recovered to reach in 2010 almost the same flux level it had in 2000. The earliest available X-ray observation (*Einstein*, Wilkes et al. 1994) caught the source in a relatively low-flux state in 1979. *ROSAT* observed the source twice (PSPC: Forster & Halpern 1996; Lawrence et al. 1997; HRI: Brandt et al. 1999) at flux levels comparable to the highest fluxes observed with *XMM-Newton*. A further *ASCA* observation is not shown here as it was simultaneous with the *ROSAT* HRI monitoring campaign (Leighly et al 1999a and 1999b).

The *XMM-Newton* observations provide simultaneous photometric data in the UV via the OM. The X-ray and UV monochromatic fluxes from all *XMM-Newton* observations are reported in Table 1. The monochromatic 2 keV (rest-frame) flux varies by a factor ~ 260 between observations XMM(2) and XMM(3). The UV variations, however, have much smaller amplitude and they are not strongly correlated with the X-ray ones. In fact, the maximum UV

¹ <http://xmm.esa.int/sas/current/howtouseasas.shtml>

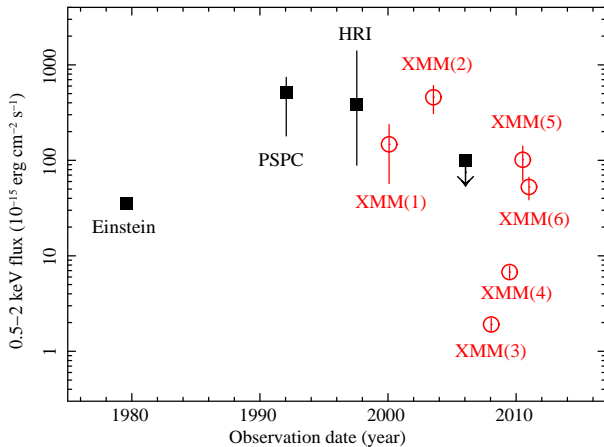


Figure 1. The historical 0.5–2 keV X-ray flux of PHL 1092. Open symbols represent the *XMM-Newton* observations discussed in our paper. The data points represent the mean flux level during the observation, and the error is a measure of the intra-observation variability rather than of the statistical error on the mean flux. The upper limit is from an *XMM-Newton* slew in 2006. The Figure is an update of Fig 2 in Miniutti et al. (2009b). We refer to the caption of that Figure for further details.

variation is a $\sim 15\%$ drop of the 1519 Å (rest-frame) monochromatic flux between observations XMM(3) and XMM(4), accompanied by an X-ray flux increase by a factor ~ 4.2 . The presence of simultaneous UV and X-ray data allows us to derive reliably the optical-to-X-ray slope α_{ox} from 2000 to 2010. Here we use the standard definition of $\alpha_{\text{ox}} = \log(f_2/f_{2500}) \log(\nu_2/\nu_{2500})^{-1} = 0.384 \log(f_2/f_{2500})$ between 2 keV and 2500 Å in the rest-frame. Following Gibson, Brandt & Schneider (2008), we also define $\Delta\alpha_{\text{ox}}$ as the difference between the observed α_{ox} and that expected from the anti-correlation between α_{ox} and the 2500 Å monochromatic luminosity which implies $\alpha_{\text{ox}}^{\text{expected}} = -1.48$ for PHL 1092 (e.g. Just et al. 2007). The α_{ox} and $\Delta\alpha_{\text{ox}}$ values for each *XMM-Newton* observation of PHL 1092 are reported in Table 1. The rest-frame 2500 Å flux density we use to derive the α_{ox} and $\Delta\alpha_{\text{ox}}$ values is extrapolated from the nearest available OM filter using a spectral index of $\alpha_\nu = -0.70$ (Wu et al. 2001).

As mentioned above, PHL 1092 became suddenly extremely X-ray weak in 2008, reaching $\alpha_{\text{ox}} = -2.51$, to be compared with $\alpha_{\text{ox}} = -1.57$ in 2003 (Miniutti et al. 2009b). Our monitoring observations of PHL 1092 show that the source has recovered part of its X-ray flux since 2008. PHL 1092 is still significantly X-ray weak, but less extreme, with $\alpha_{\text{ox}} = -1.97$ in our latest observation performed in December 2010. In Fig. 2 we show $\Delta\alpha_{\text{ox}}$ as a function of the 2 keV monochromatic flux. The almost perfect linear correlation with $\log f_{2\text{keV}}$ shows that the α_{ox} variability of PHL 1092 can be entirely explained in terms of its long-term X-ray flux changes. The UV flux is almost constant (within 10% of its mean value), indicating that the large α_{ox} variability of PHL 1092 has little to do with mass accretion rate variations, and is instead related to physical processes affecting the X-ray part of the SED only. Notice that $\Delta\alpha_{\text{ox}}$ can be used to obtain the factor $f_{\text{X-weak}}$ by which a given quasar is X-ray weak via $f_{\text{X-weak}} = 10^{-\Delta\alpha_{\text{ox}}/0.384}$. We then infer that PHL 1092 was X-ray weak by a factor $f_{\text{X-weak}} \simeq 480$ in its lowest X-ray flux state as observed during XMM(3) in January 2008.

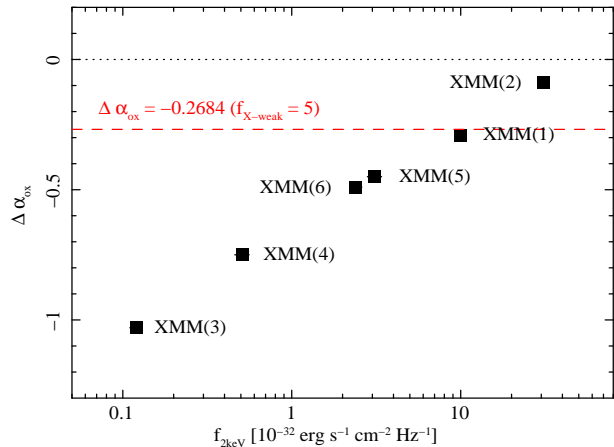


Figure 2. The 2000–2010 $\Delta\alpha_{\text{ox}}$ of PHL 1092 as a function of its 2 keV flux density showing visually that the α_{ox} variation is entirely due to the long-term X-ray variability of PHL 1092. The level $\Delta\alpha_{\text{ox}} = 0$ corresponds to $\alpha_{\text{ox}} = -1.48$, which is that expected for a quasar with the 2500 Å monochromatic luminosity of PHL 1092. We also show as reference (dashed line) the level $\Delta\alpha_{\text{ox}} = -0.2684$, corresponding to a quasar which is X-ray weak by a factor of $f_{\text{X-weak}} = 5$. The largest variation is between observations XMM(2) and XMM(3) which differ by a factor ~ 260 at 2 keV (see Table 1). PHL 1092 was X-ray weak by a factor $f_{\text{X-weak}} \simeq 480$ during XMM(3).

4 UV AND OPTICAL SPECTRA

As mentioned above, we obtained optical spectra with the Hobby–Eberly Telescope (HET) quasi-simultaneously with observation XMM(3) and between observations XMM(5) and XMM(6), on 2008 January 30 and 2010 October 31, respectively. The 2008 observation was also complemented by a second optical spectrum taken on 2008 February 14 at the William Herschel Telescope (WHT) to cover the Mg II region. Below, we start our discussion of the optical/UV properties of PHL 1092 with a qualitative analysis of the properties of the *Hubble Space Telescope* (HST) spectrum of PHL 1092 obtained in 2003.

4.1 The HST UV spectrum

PHL 1092 was observed with the HST Space Telescope Imaging Spectrograph (STIS,) on 2003 August 20 and 2003 September 18, about one and two months after the XMM(2) observation. The observations were performed with the G140L and G230L gratings covering the 1150–3180 Å spectral range. No significant variability is detected between the two HST spectra. Here we do not perform any detailed scientific analysis of the HST spectrum, but use it for illustration purposes only. In the upper panel of Fig. 3 we show the Ly α to C III] portion of the spectrum of PHL 1092 and of the HST composite for radio-quiet sources (Telfer et al. 2002). The high-ionisation C IV emission line of PHL 1092 is much weaker than in the average quasar. The C IV line is also broad and highly blueshifted with virtually no contribution at the line’s rest-frame wavelength (see Wu et al. 2011). Inspection of the optical spectrum of PHL 1092 taken at the WHT on 2008 February 14 reveals that the low-ionisation Mg II emission line is instead centred at its rest-frame wavelength and is relatively narrow, with a likely smaller contribution from a broad blueshifted component. The bottom panel of Fig. 3 shows a comparison of the C IV and Mg II line profiles in velocity space. The two observations are not simultane-

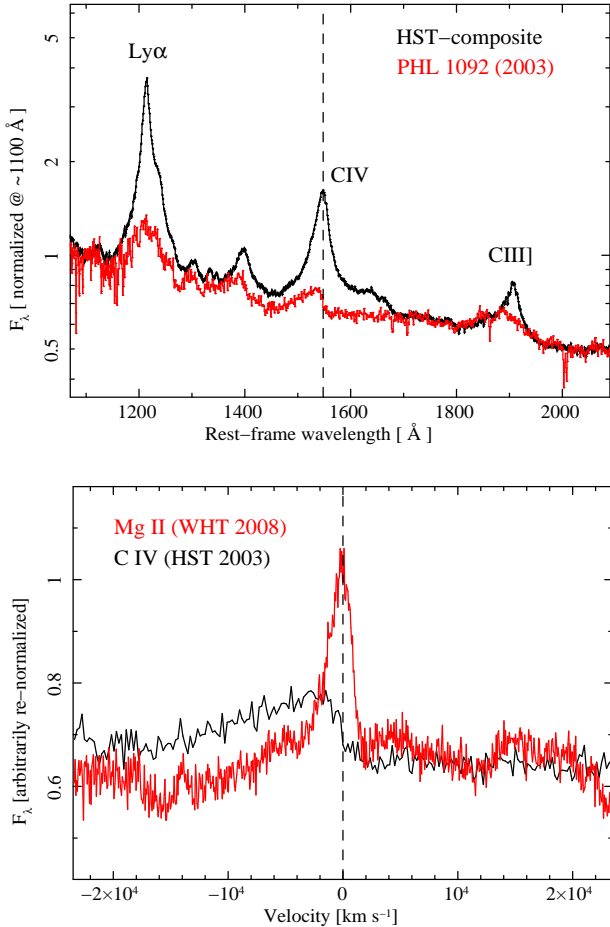


Figure 3. Top: The HST–STIS spectrum of PHL 1092 is compared with the HST–composite spectrum of radio–quiet quasars. Notice especially the weak, broad, and blueshifted C IV emission line of PHL 1092. We show as reference the rest–frame C IV wavelength of 1548 Å as a dashed line. **Bottom:** Comparison between the C IV and Mg II line profiles obtained in 2003 (HST) and 2008 (WHT) respectively. The zero velocity is shown for reference as a dashed line.

ous. C IV is from the 2003 HST observation while Mg II is from our 2008 February 14 observation with the WHT.

The purpose of showing here the HST spectrum of PHL 1092 and the remarkably different line profiles of C IV and Mg II is to associate PHL 1092 with other likely similar sources. The unusual UV emission–line properties of PHL 1092 match those of the prototypical intrinsically X–ray weak quasar PHL 1811 (Leighly et al. 2007a, 2007b), and of the two strong Fe II emitters and relatively X–ray weak NLS1 galaxies 1H 0707–495 and IRAS 13224–3809 (Leighly & Moore 2004; Leighly 2004). Leighly (2004) associates the broad, blueshifted, high–ionisation lines (e.g. C IV) with a wind, while the narrow, rest–frame, low–ionisation lines are likely produced in the denser disc or at the base of the wind itself. The lack (or extreme weakness) of any narrow C IV emission line at the rest–frame wavelength in all these sources suggests that the continuum irradiating the narrow and low–ionisation line–emitting region has been filtered through the wind, thus supporting the idea that Mg II and similar low–ionisation lines are emitted further away than the wind launching site, which Leighly estimates to be $\sim 5 \times 10^3 r_g$ for 1H 0707–495 and IRAS 13224–3809.

Most of the peculiar optical/UV properties of PHL 1811,

1H 0707–495 and IRAS 13224–3809 can be explained with a soft ionising SED depleted of X–ray photons and, at least in the case of the two latter NLS1 galaxies, by enhanced metallicity (Leighly 2004; Leighly et al. 2007b). The situation seems similar in PHL 1092: we observe weak, blueshifted C IV emission, likely produced in a wind. No narrow C IV emission line at rest–frame wavelength is observed, while Mg II is relatively strong and narrow, supporting a filtered continuum in PHL 1092 as well.

The C IV emission line properties of PHL 1092 strongly suggest the presence of a wind in August/September 2003, i.e. the epoch of the HST observation. Considering the wind launching radius estimated by Leighly for 1H 0707–495 and IRAS 13224–3809, the physical distance of the wind from the centre is ~ 50 light days in PHL 1092.² Hence, taking into account this timescale, the C IV emission corresponds to a nuclear SED which is likely similar to that we observe in July 2003 during XMM(2), when PHL 1092 was not X–ray weak ($\Delta\alpha_{\text{ox}} \sim -0.09$). We conclude that a wind in PHL 1092 can likely be launched even if the source is only moderately (or even not at all) X–ray weak.

4.1.1 Evidence for C IV variability?

All UV fluxes obtained with the OM during our monitoring show signs of modest long–term variability, with a tendency of lower variability amplitude at longer wavelengths (see Table 1). The last three XMM–Newton observations have exposures in multiple filters. The variability trend above 1655 Å (M2 filter) is for a higher flux in XMM(4) a decrease in XMM(5) and a final rise in XMM(6). On the other hand, the trend for the shortest wavelength W2 filter is, surprisingly, the opposite. It is crucial to note that the OM filter W2 has an effective rest–frame wavelength of 1519 Å, which coincides with the wing of the (blueshifted) C IV emission line of PHL 1092.

In Fig. 4 we show the HST spectrum of PHL 1092 in the restricted region around the C IV emission line on which we overplot the monochromatic OM fluxes from the W2 (1519Å) and M2 (1655Å) filters for the three observations with multiple–filter exposures. As the HST spectrum was obtained at a time when PHL 1092 was most likely not particularly X–ray weak, we have re–normalised the HST spectrum to the OM photometry of the least X–ray weak observation XMM(5). As can be seen, the HST spectral shape is consistent with the OM photometry during XMM(5) and XMM(6), as shown by the open diamonds and filled squares in Fig. 4. On the other hand, this is not the case for the X–ray weakest observation XMM(4), in which the two OM filters have a flux consistent with each other (open circles in the Figure).

This comparison suggests significant UV spectral variability. In particular, our result suggests that the C IV emission line was either much fainter or more blueshifted during the X–ray weak state observation XMM(4). Both possibilities (and of course a combination of them) can explain the difference between the HST spectral shape and the OM photometry during XMM(4). In fact, there are numerous suggestions in the literature that the C IV line equivalent width (EW) is anti–correlated with its blueshift (e.g. Richards et al. 2011) and that sources with smaller C IV EW (and/or larger blueshift) are typically X–ray weaker or *soft–spectrum* objects (Wu et al. 2009; Kruczek et al. 2011; Richards et al. 2011). Our result suggests that the idea that X–ray weaker quasars have lower

² We assume here a black hole mass of $3 \times 10^8 M_{\odot}$, see e.g. Nikołajuk, Czerny & Gurynowicz (2009).

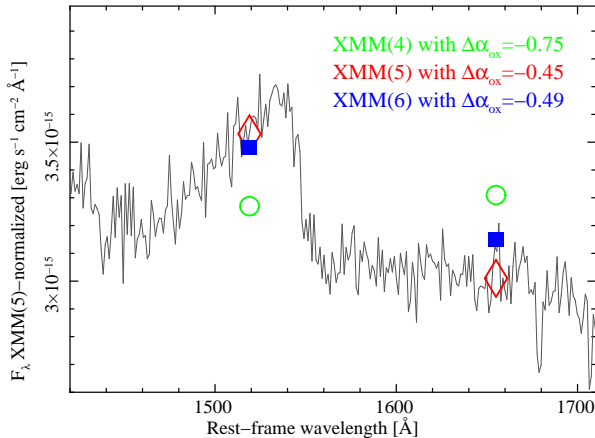


Figure 4. The HST spectrum of PHL 1092 normalised to the XMM(5) OM photometric data around the C IV emission line is shown with the OM monochromatic fluxes at 1519 Å and 1655 Å, corresponding to observations XMM(4), XMM(5), and XMM(6), which are the only ones to have multiple-filter exposures. The $\Delta\alpha_{\text{ox}}$ for each observation is also reported as reference. We use open circles for XMM(4), open diamonds for XMM(5), and filled squares for XMM(6).

C IV EW and larger C IV blueshift possibly holds not only statistically in large AGN samples, but also in individual sources such as PHL 1092. Unfortunately, the lack of multiple-filter exposures during the X-ray weakest observation XMM(3) prevents any further analysis of the issue. A UV spectrum of PHL 1092 during an extreme X-ray weak epoch would clearly solve this important issue.

4.2 Optical HET spectra: comparison between the 2008 and 2010 observation

The 2008 HET and WHT optical spectra of PHL 1092 from Mg II to H β were presented and qualitatively discussed by Miniutti et al. (2009b). The main conclusion was that, despite the enormous X-ray flux drop, the optical spectra did not show significant changes with respect to older spectra (e.g. Bergeron & Kunth 1980). Here we compare the two HET optical spectra of PHL 1092 which were obtained in 2008 and 2010. The X-ray flux density at 2 keV increased by a factor ~ 20 from 2008 to 2010.

Spectra of PHL 1092 were taken on two occasions (2008 January 28 and 2010 October 31) with the Low Resolution Spectrograph (LRS; Hill et al 1998) on the HET (Ramsey et al 1998, Shetrone et al 2007). On each night two 600 s exposures were obtained with a $1.0''$ slit and the 600 line mm^{-1} grating. The calibrated spectra, which have a resolution of ≈ 5 Å, are displayed in Fig. 5 in a restricted region covering some of the Fe II complex as well as the H β and [O III] emission lines. The spectra were placed on an approximate absolute flux scale by combining photometry taken by the Sloan Digital Sky Survey (SDSS; York et al 2000) with the *R*-band images taken by the LRS immediately before the acquisition of the spectra. SDSS photometry in the *ugriz* filters (Fukugita et al 1996) of the field containing PHL 1092 was obtained on 2004 December 14. We derived the *R* to *r* transformation using field stars (employing *r* – *i* as the colour term). As shown in Fig. 5, the two HET spectra are quite similar in continuum shape and line properties; the major change during this 2.8 yr span (2 yr in the quasar rest-frame) is a lowering of the flux level by 0.14 mag accompanied by a similar drop of the H β line flux. This overall flux

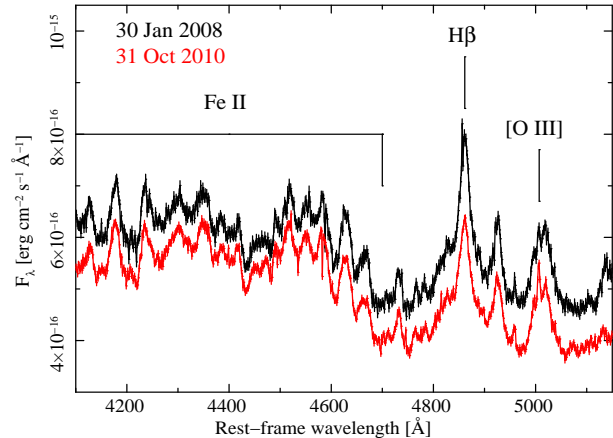


Figure 5. The HET spectra of PHL 1092 from the 2008 and 2010 observations. We do not show here the WHT data (obtained just 15 days after the 2008 HET data) as the WHT and HET spectra are consistent with each other in the common spectral range.

change is roughly consistent with that observed in the UV from the quasi-simultaneous OM photometry (see Table 1).

5 X-RAY SPECTRAL ANALYSIS I: BASIC SPECTRAL CHARACTERISATION

Having established that the extreme α_{ox} variation of PHL 1092 is due to its long-term X-ray variability only (see Fig. 2), we turn to the *XMM-Newton* data with the goal to explain simultaneously the UV-to-X-ray SED of PHL 1092 at all observed flux levels. As mentioned, no X-ray spectral information is available for XMM(1), so we perform our analysis considering observations XMM(2) to XMM(6) spanning 7.5 yr (5.4 yr in the rest-frame) in the activity of PHL 1092 and more than two orders of magnitude in soft X-ray flux. All EPIC-pn data are considered between 0.3 keV and up to the energy at which the source is confidently detected above the background. The EPIC-pn spectra used in our analysis are shown in Fig. 6.

We first perform a basic phenomenological spectral analysis of the X-ray data, which are all fitted simultaneously here as well as in all subsequent Sections. As discussed by Gallo et al. (2004), Dasgupta et al. (2004), and Miniutti et al. (2009b), the X-ray spectrum of PHL 1092 can be described by the combination of a high-energy power law plus a soft excess component. Here we adopt a standard multi-colour blackbody (the DISKBB model, see e.g. Mitsuda et al. 1984) and power-law model to describe the spectra in all observations, i.e. at all X-ray flux levels. We assume Galactic absorption with column density fixed to the value taken from Kalberla et al. (2005), namely $3.57 \times 10^{20} \text{ cm}^{-2}$. As the power law slope cannot be constrained reliably in all observations we (arbitrarily) force the photon index to be the same in all observations. We obtain a fair phenomenological representation of the spectra ($\chi^2/\text{dof} = 425/357$) with $\Gamma = 2.0 \pm 0.3$. The blackbody has a temperature in the range of $\sim 0.08 - 0.12$ keV, consistent with the soft excess temperature of type 1 AGN (e.g. Czerny et al. 2003; Gierliński & Done 2004; Miniutti et al. 2009a). We stress here that the blackbody component should not be identified with thermal disc emission, as extrapolation down to the UV underestimates the OM data by more than 2 orders of magnitude. The results of this phenomenological description of the X-ray data are

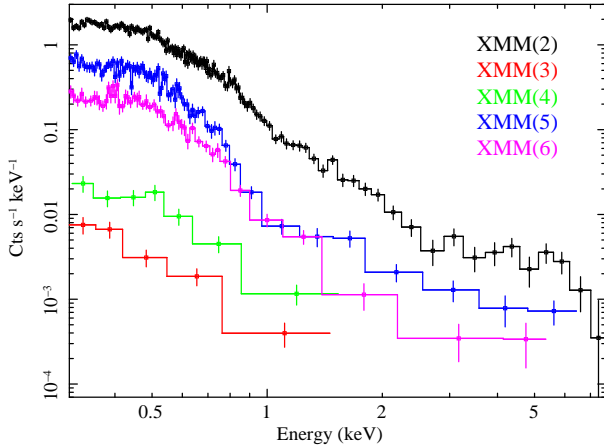


Figure 6. The EPIC-pn spectra of PHL 1092 used in our analysis from 2003 to 2010. All data are considered down to 0.3 keV and up to the observation-dependent energy at which the source is confidently detected above the background level. Observation XMM(1) is not considered here as no spectral data are available. The x-axis energy is in the observed frame here and in all subsequent figures, unless specified otherwise.

reported in Table 2. In the following Sections, we explore a set of more physically-motivated spectral models applied simultaneously to the EPIC and OM data.

6 X-RAY SPECTRAL ANALYSIS II: BASELINE MODEL

We adopt as our baseline model the recently developed OPTXAGN model (see Done et al. 2012; Jin et al. 2012 for a detailed description and applications). This model assumes that the disc emits, at each radius, a colour-temperature corrected blackbody down to a given X-ray corona outer radius R_c . The main model assumption is that the energy can no longer thermalise within R_c , and is instead distributed between powering the soft X-ray excess component and the high energy power-law tail via Comptonization in a two-phase plasma. The energy distribution within the corona is determined by the fraction of coronal luminosity powering the high-energy power-law f_{pl} (the remaining coronal luminosity $1 - f_{\text{pl}}$ powers the soft excess). As mentioned, R_c sets the X-ray corona outer radius, while its inner boundary coincides with the innermost stable circular orbit (ISCO) R_{ISCO} . The total coronal luminosity is proportional to $1 - R_{\text{ISCO}}/R_c$ so that no X-ray emission is produced if $R_c \leq R_{\text{ISCO}}$.

6.1 Soft excess as Comptonization

The first spectral model we consider is the baseline OPTXAGN model in which the soft excess is due to the Comptonization of the soft disc thermal photons in an optically thick plasma. As the disc thermal component contributes in the UV, all the available OM data are used simultaneously with the EPIC spectra to constrain the thermal disc emission. As we fit simultaneously UV and X-ray data, we include the REDDEN (for UV data) and PHABS (for X-ray data) models to account for line-of-sight Galactic absorption. We use the standard dust-to-gas conversion $E(B-V) = 1.7 \times 10^{-22} N_{\text{H}}$ (Bessel 1991) to link the UV and X-ray absorption.

Our goal is to reproduce the UV/X-ray data in all observations with variations of a minimum number of parameters. As the UV flux of PHL 1092 does not vary significantly (see Table 1), we

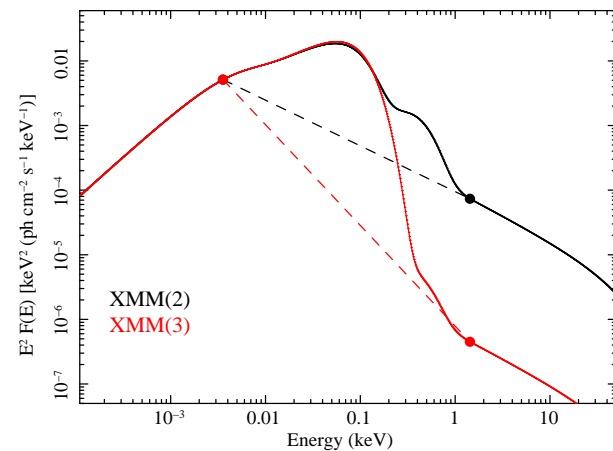
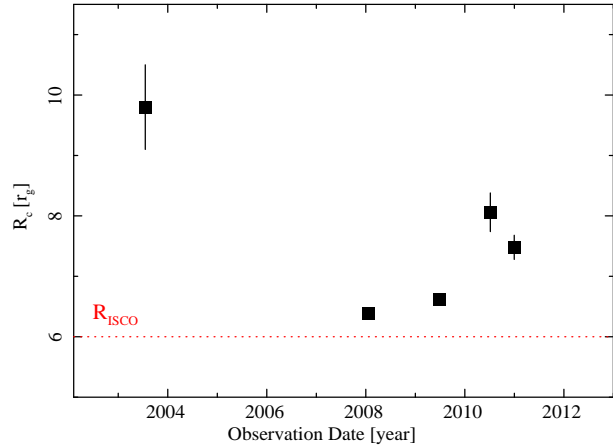


Figure 7. Top: The X-ray corona outer boundary R_c as a function of time in PHL 1092 for the case of a Schwarzschild BH with $a = 0$ and $R_{\text{ISCO}} = 6 r_g$. The collapse of the corona down to $\sim R_{\text{ISCO}}$ is able to explain the factor of ~ 260 X-ray flux drop between the highest and lowest flux observations (2003 and 2008) at fixed Eddington ratio. **Bottom:** The $E^2 F(E)$ model SED of PHL 1092 during the highest and lowest flux observations XMM(2) and XMM(3) as obtained with the baseline model for $a = 0$ (see Table 3, top). The SED has been corrected for Galactic absorption. We also show as filled circles the position of 2500 Å and 2 keV in the rest-frame. The dashed lines represent the optical to X-ray spectral slope for the two observations.

force the Eddington ratio to be the same at all X-ray flux levels, i.e. in all observations³. Given that the phenomenological model explored above indicates a similar spectral shape of the soft excess in all observations (see Table 2), we also assume that the electron temperature (kT_e) and optical depth (τ_e) of the optically-thick plasma producing the soft excess are constant. One of the model parameters is the BH spin, and we consider two different cases, namely a non-rotating Schwarzschild BH ($a = 0$) and a maximally spinning Kerr BH ($a = 0.998$). The difference between the two cases is that the innermost stable circular orbit is $R_{\text{ISCO}} = 6 r_g$ for $a = 0$ and $1.24 r_g$ for $a = 0.998$ (where $r_g = GM_{\text{BH}}/c^2$).

We are thus left with the following free parameters: the BH

³ Our assumption was checked a-posteriori. Indeed, if we instead assume observation-dependent Eddington ratios, they all appear to be consistent within the errors with that obtained by forcing it to be the same in all observations (Table 3).

mass, the Eddington ratio, kT_e , τ_e , Γ_h , the outer X-ray corona radius R_c , and the fraction of coronal luminosity powering the hard power-law f_{pl} . However, all these parameters are forced to be the same in all observations except R_c , Γ_h , and f_{pl} . After a few initial tests, we found that the data are best represented if Γ_h is forced to be the same in the first three and last two observations.

We obtain a fair (although not excellent) simultaneous description of the OM and EPIC-pn data for both the $a = 0$ and $a = 0.998$ cases, with $\chi^2/\text{dof} = 480/370$. The results are reported in Table 3. We obtain a BH mass of $\sim 2.4 \times 10^8 M_\odot$ for the $a = 0$ case and $\sim 1.7 \times 10^9 M_\odot$ for the $a = 0.998$ one. The corresponding Eddington ratios imply super-Eddington accretion for a Schwarzschild BH with $L/L_{\text{EDD}} \sim 2.45$, and a sub-Eddington ratio of $L/L_{\text{EDD}} \sim 0.31$ for a Kerr one. Using the standard mass scaling relations (e.g. Vestergaard & Peterson 2006) together with the optical luminosity and the FWHM of H β obtained from single-epoch optical spectra, one estimates a black hole mass of $\sim 3 \times 10^8 M_\odot$ for PHL 1092, in line with our best-fitting result for the Schwarzschild BH case (Nikołajuk, Czerny & Gurynowicz 2009).

The most striking results of our analysis are that i) the X-ray corona of PHL 1092 is extremely compact at all probed X-ray flux levels with $R_c \leq 1.8 \times R_{\text{iscco}}$ in all observations, and ii) the extreme observed X-ray and α_{ox} variability can be explained in terms of a variation of the X-ray corona size and hence X-ray output (proportional to $1 - R_{\text{iscco}}/R_c$). The deep minimum X-ray flux state observed during XMM(3) is the result of an almost complete collapse of the X-ray corona down to the inner disc boundary R_{iscco} in both the Schwarzschild and Kerr cases.

The evolution of R_c is shown in the top panel of Fig. 7 for the Schwarzschild BH case⁴. In the bottom panel, we show the (unabsorbed) model SED showing visually the difference in the corona X-ray output at the two extreme flux levels, accounting for the large variation of α_{ox} from -1.57 to -2.51 . The nominal power-law connecting 2500 Å and 2 keV in the rest-frame is also shown as a dashed line in both cases. Since we assume that the Eddington ratio is constant, the bolometric luminosity is the same at all X-ray flux levels, namely $L_{\text{Bol}} \sim 4.7 \times 10^{46} \text{ erg s}^{-1}$. This implies an enormous change in the X-ray bolometric correction (K_X), from $K_X \sim 8 \times 10^2$ in the highest flux XMM(2) observation to $K_X \sim 1.2 \times 10^5$ in the lowest flux XMM(3) one for the standard 2–10 keV X-ray band.

6.2 Can X-ray absorption make PHL 1092 a standard quasar with constant $\Delta\alpha_{\text{ox}} \sim 0$?

The model presented above successfully explains the α_{ox} variation but at the expense of invoking a *breathing* X-ray corona producing an intrinsic X-ray flux change of more than two orders of magnitude from the highest to the lowest flux state of PHL 1092. Here we search for a solution in which the intrinsic X-ray flux of PHL 1092 is constant and possibly similar to that expected for a quasar with its optical luminosity. Guided by the observational fact that X-ray weak quasars are often associated with intrinsic UV and X-ray absorption (at least the BAL X-ray weak sources), we assume that the X-ray flux variability of PHL 1092 is apparent and due to X-ray absorption.

⁴ The Kerr BH case is qualitatively the same and we discuss here the Schwarzschild case only for simplicity. In fact, the evolution of R_c in the two cases is almost identical, once expressed in units of R_{iscco} .

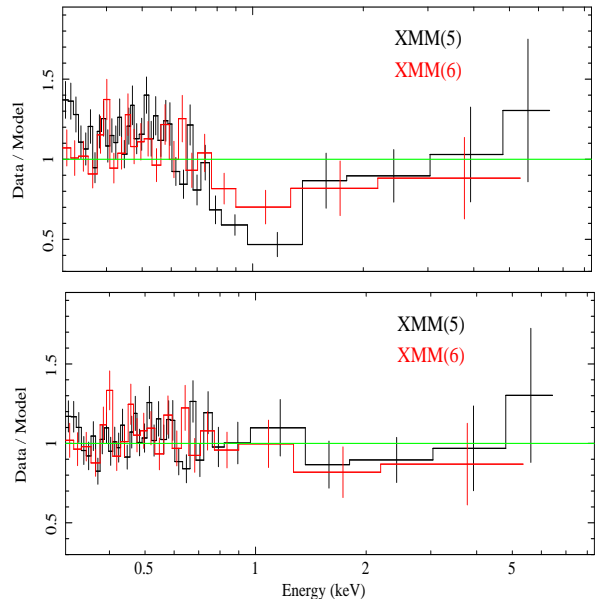


Figure 8. Top: The data-to-model ratio for the intermediate-flux observations XMM(5) and XMM(6) using a single absorption model. **Bottom:** Same as above but including a Gaussian absorption line at $E_{\text{abs}} \sim 1.05$ keV. We only show the intermediate-flux observations for visual clarity as the absorption feature is more prominent in these data sets (see text for details). The feature is marginally visible in XMM(2) as well, while the data from XMM(3) and XMM(4) are inconclusive due to the relatively poor quality around 1 keV. The data have been re-binned for visual clarity only.

To test this scenario in PHL 1092, we use the same model as above, adding a partially ionised X-ray absorber with no counterpart in the UV. As our absorption spectral model (the ZXIPCF model, Reeves et al. 2008) is only defined in the X-ray band, we use the EPIC data only, fixing the BH mass and Eddington ratio to the values derived above, so that the UV data are automatically described by the overall model (provided that $R_c \leq 20 - 30 r_g$). We discuss here for simplicity the Schwarzschild $a = 0$ case only (qualitatively similar results are obtained in the Kerr case). Our goal is to reproduce the X-ray weakness and variability of PHL 1092 with absorption effects. Hence, we force the corona outer boundary R_c to be the same in all observations. This implies that the intrinsic X-ray flux of PHL 1092 is always the same. For self-consistency, the absorber ionisation state is also forced to be the same at all flux levels although, in principle, the ionising flux may intercept clouds with different density at different times. The coronal parameters affecting the soft excess (kT_e and τ_e) and the high-energy power-law tail (Γ_h and f_{pl}) are also forced to be constant to limit further the number of free parameters (forcing the coronal parameters to be the same in all observations reduces the number of free parameters from 27 to 11).

After a few tests, we found that the absorber column density and covering fraction cannot be simultaneously constrained. We then decided to force a marginally Compton-thick column density of $N_{\text{H}} = 10^{24} \text{ cm}^{-2}$ in all observations and let the covering fraction vary. This choice is motivated by the fact that our absorption model neglects Compton scattering, thus becoming less robust for much higher column densities. On the other hand, after testing different N_{H} values, we find that a significantly lower N_{H} cannot reproduce the observed large X-ray flux variability with changes in covering fraction only. Changing the column density around the chosen value slightly affects the best-fitting ionisa-

tion state and covering fraction but not the overall statistical quality of the fit. Hence, the derived parameters must be taken with caution. We do not find a fair description of the EPIC data ($\chi^2/\text{dof} = 710/362$). It should, however, be stressed that most of the contribution to the χ^2 comes from the intermediate-flux observations XMM(5) and XMM(6), which appear to exhibit a further absorption structure at ~ 1 keV (~ 1.4 keV in the rest-frame). The absorption feature is shown in terms of data-to-model ratio for the intermediate-flux observations XMM(5) and XMM(6) in the top panel of Fig. 8.

To address this feature, we added a Gaussian absorption line with the same energy and width in all observations, but we allow the absorption line optical depth to be observation-dependent. We obtain a good description of the data ($\chi^2/\text{dof} = 410/355$) with a relatively broad absorption line ($\sigma_{\text{abs}} \sim 0.20$ keV) at $E_{\text{abs}} \sim 1.05$ keV in the observed-frame, corresponding to ~ 1.47 keV in the rest-frame. The line is more prominent in XMM(5) and XMM(6) with optical depths of $\tau_{(5)} = 1.00 \pm 0.10$ and $\tau_{(6)} = 0.60 \pm 0.10$ (see the bottom panel of Fig. 8). It is also detected in the highest flux observation XMM(2) with $\tau_{(2)} = 0.15 \pm 0.03$; it is not detected in the lowest flux observations, where the signal-to-noise-ratio around 1 keV is, however, limited. The broad width and energy of the absorption line suggests an identification with the Fe L absorption complex around 1 keV, with possible contribution from Ne IX-X and/or Mg XI-XII (see e.g. Nicastro, Fiore & Matt 1999). Identification of the absorption feature with Fe L resonant absorption at ~ 1 keV implies an outflow with highly relativistic velocity $v_{\text{out}} \sim 0.3 c$.

On the other hand, the X-ray flux variability is produced by the variation of the covering fraction of a relatively cold ($\log \xi \leq -1.0$) absorber with $N_{\text{H}} = 10^{24} \text{ cm}^{-2}$ (fixed, as discussed above). The absorber covers $\sim 19\%$ of the X-ray source in the highest X-ray flux observation, and $\sim 99.6\%$ of it during the lowest X-ray flux one. The best-fitting parameters for our spectral decomposition are reported in Table 4. The evolution of the cold absorber covering fraction is shown in Fig. 9 (top). In the bottom panel of Fig. 9, we show the model X-ray SED for the highest and lowest X-ray flux states together with the intrinsic X-ray corona output (common to all flux states).

Remarkably, if the absorber were absent, the intrinsic monochromatic flux of PHL 1092 at 2 keV would be a factor ~ 1.3 higher than that observed in the high flux state. Such unabsorbed intrinsic X-ray flux makes PHL 1092 a standard quasar with constant $\Delta\alpha_{\text{ox}} = -0.05 \simeq 0$. Thus, within the context of the absorption model, PHL 1092 would be a quasar with standard X-ray output, which only appears extremely X-ray weak at times due to intervening absorption.

7 X-RAY SPECTRAL ANALYSIS III: THE NATURE OF THE SOFT EXCESS

In the previous Sections, we have assumed that the soft X-ray excess is produced by Compton up-scattering of the UV/EUV disc photons in an optically thick corona with temperature ~ 0.15 keV. This interpretation of the soft excess has been frequently questioned by many different authors (e.g. Gierliński & Done 2004) because, in order to reproduce the uniform spectral shape in samples of AGN with significantly different BH mass and Eddington ratio, the electron temperature must be remarkably uniform. The uniform soft excess shape may indicate that processes that are independent of accretion physics are instead at play. Below, we ex-

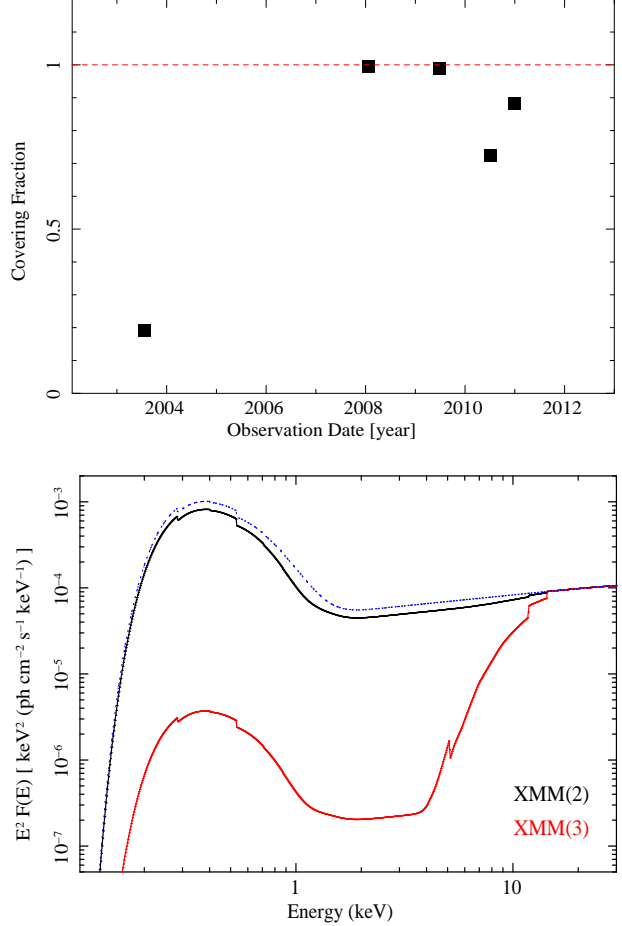


Figure 9. **Top:** The evolution of the absorber covering fraction with time. The lowest flux states observed in 2008 and 2009 are due to the $\sim 100\%$ covering of the X-ray source. **Bottom:** The $E^2F(E)$ model SED of PHL 1092 during the highest and lowest flux observations XMM(2) and XMM(3) as obtained with the absorption model. The ~ 1 keV absorption line in XMM(2) is broad and has relatively low equivalent width, so it is not clearly seen on this scale. We also show, with a dotted line (blue on-line), the unabsorbed intrinsic X-ray flux which is the same in all observations.

plore two spectral models in which the soft X-ray excess is either an apparent feature due to intervening absorption or a real extra emission component due to X-ray reflection off the inner accretion disc. Both interpretations invoke atomic processes to explain the nature of the soft excess and, as such, they naturally provide an explanation for the uniform shape of this feature in AGN X-ray spectra.

7.1 Partially ionised absorption

As mentioned above, a partial covering X-ray absorption model can reproduce the extreme α_{ox} variability of PHL 1092. Moreover, it also explains its X-ray weakness since, if the absorber was absent, PHL 1092 would be a quasar with standard X-ray output and $\Delta\alpha_{\text{ox}} \sim 0$. Here we explore the possibility that the ionised absorber also accounts for the X-ray soft excess. We use exactly the same model as above but we force the X-ray corona to only power the high-energy power-law by fixing $f_{\text{pl}} = 1$ in all observations. This model eliminates the optically thick X-ray corona generating the soft excess which has thus to be explained with a different pro-

cess. In this case we assume that the soft X-ray excess is not a real extra emission component, but rather an apparent feature due to deep absorption troughs affecting the intermediate X-ray energy band ($\sim 0.7 - 2$ keV).

The model, however, does not reproduce the data ($\chi^2/\text{dof} = 750/358$). Even if the Gaussian absorption line is replaced with a highly ionised outflowing absorber, the quality of the fit remains unacceptable, and the power law photon index reaches an implausibly high value of $\Gamma \sim 3.8$. In fact, the only way to obtain a fair description of the data within this model is to allow for a large intrinsic X-ray flux variation, i.e. for a variation in the corona size set by R_c . In this context, as the intrinsic flux varies, we also leave the absorber(s) ionisation free to vary. This approach produces a fit with good statistical quality ($\chi^2/\text{dof} = 420/354$), and the soft excess is reproduced. However, the model implies that the intrinsic X-ray flux of PHL 1092 changes by a factor ~ 250 between the highest and lowest flux states. Moreover, the ionisation state of the absorbers does not follow the unabsorbed flux, although this may be understood by considering that the ionising flux may intercept clouds of different density and/or distance at different times. The model fails at reproducing via absorption effects any of the observed X-ray flux and α_{ox} variability; it is just a modified version of the baseline model. The only difference between the present and baseline models is in the description of the nature of the soft excess rather than in the mechanism behind the extreme X-ray variability. Much higher quality existing X-ray data sets are better suited to attack the issue of the nature of the soft excess. Hence, we do not discuss this model any further here. We point out, however, that our absorption model does not include re-emission, which is likely to mostly contribute in the soft X-ray band and may be of some help in reproducing the soft excess for specific geometries (e.g. Schurch, Done & Proga 2009).

7.2 Ionised disc reflection

We now consider the possibility that the soft X-ray excess is a real extra emission component affecting primarily the soft X-ray band. The most attractive idea, besides Comptonization, is that ionised reflection off the inner accretion disc contributes to the soft X-rays. X-ray reflection off the inner accretion disc has been shown to represent a plausible explanation of the nature of the soft excess in many sources and, in particular, in many NLS1 galaxies (e.g. 1H 0707-495, Fabian et al. 2004, 2009; NGC 4051, Ponti et al. 2006; IRAS 13224-3809, Ponti et al. 2010).

We apply the baseline OPTXAGN model as above to all EPIC data fixing the BH mass and Eddington ratio to the best-fitting values derived with the baseline model, depending on the adopted BH spin. We also force the X-ray corona to only power the hard X-ray power-law ($f_{\text{pl}} = 1$) so that the baseline model does not produce any soft excess. To describe the soft X-ray excess as ionised disc reflection, we use the the REFLION model (Ross & Fabian 2005) to which we apply the RDBLUR/KDBLUR relativistic kernel, appropriate for a Schwarzschild/Kerr BH, and obtained by R. Johnstone and A.C. Fabian from the DISKLINE/LAOR models (Fabian et al. 1989; Laor 1991). As the corona is now optically thin, the inner disc below R_c is visible and we fix the inner disc radius to R_{ISCO} at all flux levels.

The model free parameters are thus R_c , the hard X-ray power law photon index Γ_h , the reflection emissivity index q (where the emissivity profile is $\propto r^{-q}$), the disc inclination i , and the reflection ionisation state ξ_{ref} and normalisation. However, q and (obviously) i are forced to be the same at all flux levels. To limit fur-

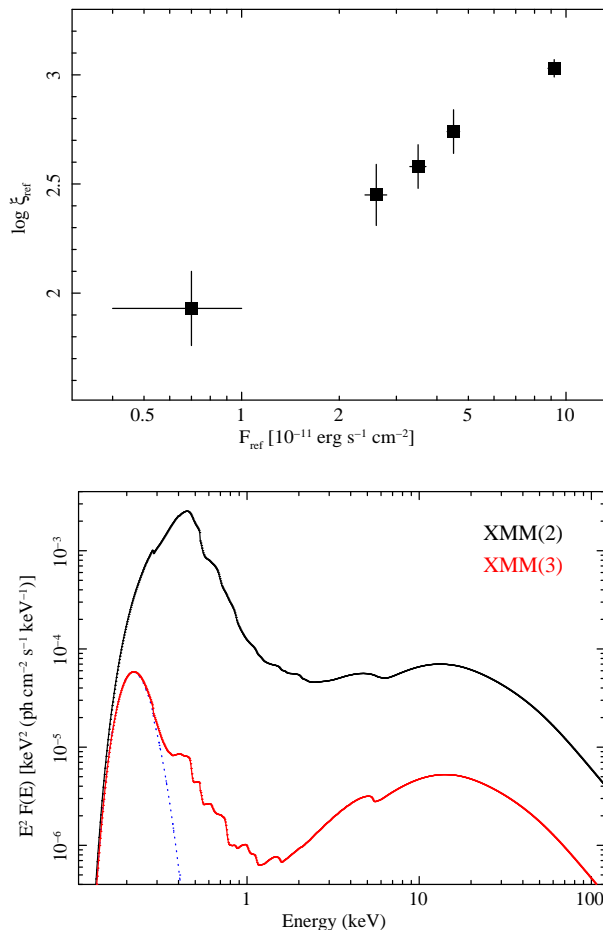


Figure 10. Top: The correlation between the accretion disc ionisation state and the total reflection flux F_{ref} . Since F_{ref} is proportional to the flux irradiating the disc, the excellent correlation shows that the model self-consistently accounts for irradiating flux and ionisation changes. **Bottom:** The $E^2 F(E)$ model X-ray SED of PHL 1092 during the highest and lowest flux observations XMM(2) and XMM(3) as obtained with the disc reflection-dominated model. The SED has been corrected for the intrinsic warm absorption, while Galactic absorption is present. The X-ray SED is completely reflection-dominated with some accretion disc contribution at soft X-rays (blue dashed line) which becomes visible in the low X-ray flux observations.

ther the number of free parameters we attempted to force Γ_h to be constant, but we found that the last three observation do require a steeper index than the others; we thus force Γ_h to be the same in the first two and last three observations, respectively. Our initial fits show that the X-ray spectrum of PHL 1092 is completely reflection-dominated at all flux levels. We thus force the corona outer radius R_c to coincide with R_{ISCO} so that no X-ray corona emission is present.

We obtain a fair description of the data ($\chi^2/\text{dof} = 420/353$ for the Kerr BH case and $\chi^2/\text{dof} = 455/353$ for the Schwarzschild BH case) with the inclusion of a low-column/low-ionisation warm absorber. As we obtain a better description of the data with a maximally spinning Kerr BH, we only discuss the $a = 0.998$ case here. For the warm absorber, we use the ZXIPCF model fully covering the source. our results are reported in Table 5. We must point out that the warm absorber component is not exceedingly robust as it is affected by the presence of the thermal disc emission, which impacts the softest X-ray energies. The latter

component is not fitted but imposed by our choice of BH mass and Eddington ratio which are, as discussed later, somewhat uncertain. It is, however, reassuring that the warm absorber ionisation state is well correlated with the total flux (see Table 5), ensuring the overall self-consistency of the model. The warm absorber model improves the fitting statistics by $\Delta\chi^2 = -32$ for 6 additional free parameters.

The column F_{ref} in Table 5 refers to the total reflection flux in the 0.001–300 keV band rather than the flux in any restricted energy band. F_{ref} is at all times proportional (via the disc albedo \mathcal{A}) to the total flux irradiating the disc F_{irr} . Hence, for the model to be self-consistent, F_{ref} must be correlated with the disc ionisation state ξ_{ref} . Fig. 10 (top) demonstrates that the two quantities are extremely well correlated, so that the reflection scenario is indeed self-consistent. The key result of our modelling is shown in the bottom panel of Fig. 10, where we display the model X-ray SED for the highest and lowest flux states. The key point is that the actual reflection flux change is only a factor ~ 10 between the two flux states and not the factor ~ 260 observed at 2 keV (see Table 1). This aspect is best seen above ~ 30 keV where ionisation effects are negligible. The flux change is larger than two orders of magnitude at soft X-rays, mostly because of the different disc ionisation. Ionisation changes affect very significantly the reflection spectral shape, redistributing the flux from EUV to hard X-rays. Thus, two reflectors with exactly the same overall total flux but different ionisation may differ enormously in the flux calculated in any restricted energy band. This is exactly what happens here: the low flux reflector has a lower ionisation than the high flux one (about a factor 10), which implies larger opacity in the soft X-rays depressing the reflection flux in this band.

7.2.1 Reflection-dominated X-ray spectrum and light-bending

As seen above, the X-ray spectrum of PHL 1092 can be interpreted as being reflection-dominated at all flux levels. Reflection-dominated spectra require the selective suppression of the intrinsic continuum. As shown, for instance, by Martocchia, Karas & Matt (2000), light-bending effects can produce reflection-dominated spectra by selectively depressing the X-ray continuum at infinity while increasing the disc irradiation and hence the reflection flux. According to our own ray-tracing simulations, the X-ray spectrum becomes increasingly reflection-dominated as the X-ray primary source location approaches the BH (see Miniutti et al. 2003; Miniutti & Fabian 2004). In the case of a Kerr BH, for any distance $\leq 5 r_g$, the flux irradiating the disc is always at least twice that escaping at infinity so that reflection-dominated spectra are produced. We propose that the X-ray corona in PHL 1092 is confined within a few gravitational radii from the BH and that light-bending effects are responsible for the observed reflection-dominated spectrum.

Let us now consider the appearance of PHL 1092 in the absence of light-bending effects, for the standard case in which the X-ray corona is not confined to the strong field regime close to the BH. In such a situation 50% of the emitted X-ray flux is directed away from the disc and detected as the X-ray continuum flux F_{cont} . The remaining 50% irradiates the disc with a flux $F_{\text{irr}} = F_{\text{cont}}$ and the spectrum is not reflection-dominated. F_{irr} is then reprocessed into the X-ray reflection spectrum with flux $F_{\text{ref}} = \mathcal{A} F_{\text{irr}}$, where \mathcal{A} is the disc albedo. The remaining fraction of irradiating flux is absorbed, thermalised, and emitted in the UV as reprocessed quasi-blackbody emission. \mathcal{A} is generally a function of the incident angle, energy, and disc ionisation. However, for the purposes of our dis-

cussion we assume for simplicity that $\mathcal{A} = 0.5$, i.e. in between the typical albedo of a completely cold disc ($\sim 0.1 - 0.2$) and a fully ionised one.

Light-bending effects break the equivalence $F_{\text{irr}} = F_{\text{cont}}$, by differently affecting F_{cont} and F_{irr} , but obviously maintain $F_{\text{ref}} = \mathcal{A} F_{\text{irr}}$. Let us assume for simplicity a point-like X-ray source on the BH axis at $2 r_g$ from the BH, where F_{irr} is amplified by a factor ~ 1.5 with respect to the case with no light-bending (see e.g. Fig. 13 of Fabian et al. 2012). Under this assumption we can estimate the total flux that would be observed in the absence of light-bending effects, where the spectrum is not reflection-dominated and the disc subtends a solid angle of 2π at the source.

It turns out that the total (continuum + reflection) flux density at 2 keV in the absence of light-bending effects is higher than the observed (reflection only) by a factor ~ 70 during the low flux state and by a factor ~ 9 during the high flux one. This result implies that PHL 1092 would have had $\Delta\alpha_{\text{ox}} \sim -0.32$ in its lowest X-ray flux state and $\Delta\alpha_{\text{ox}} \sim +0.28$ in its highest. In summary, the reflection-dominated model implies that PHL 1092 would be a quasar with relatively standard X-ray output and $\Delta\alpha_{\text{ox}} \sim 0$ oscillating between X-ray weak and X-ray bright states in the absence of light-bending effects.

A final word of caution must be placed on the values of BH mass and Eddington ratio we have assumed. We have adopted the best-fitting values of our baseline model for a Kerr BH, but this approach is not entirely correct. In fact, if the X-ray spectrum is reflection-dominated, reprocessing is inevitably important in the optical/UV as well, as we expect that $(1 - \mathcal{A}) F_{\text{irr}} \sim 0.5 F_{\text{irr}}$ is absorbed and reprocessed as thermal emission in the UV. Moreover, the X-ray reflection spectrum itself contributes in the UV/EUV down to the (rather uncertain) energy where Comptonization is efficient in producing the irradiating X-ray power law. The UV outflow also certainly contributes via scattering to the UV flux. In summary, we caution that the BH mass estimated with our baseline model could actually over-estimate the true value because our model attributes the UV emission entirely to the thermal accretion disc, while other contributions are possible (if not likely).

8 A CLOSER LOOK AT THE X-RAY VARIABILITY OF PHL 1092

The soft X-ray light curves from three *XMM-Newton* observations are shown in Fig. 11 in the 0.3–1.43 keV band (~ 0.4 –2 keV in the rest-frame). The soft band is selected because the low-flux observations are background-dominated above ~ 2 keV (rest-frame) and because the count rate drops rapidly with energy due to the steep spectrum of PHL 1092, making it difficult to study the hard X-ray variability even at the highest X-ray flux levels.. We show observations XMM(2), XMM(4), and XMM(6), as they are representative of the typical X-ray variability in high, low, and intermediate flux states, respectively. One of the key properties of X-ray time series from accreting systems is the intimate relation between the variability on different timescales. As discussed by many authors (see e.g. Uttley & McHardy 2001; Uttley, McHardy & Vaughan 2005) the root-mean-square (RMS) variability for a given segment of a light curve is linearly correlated with the segment mean flux on all measured timescales. The linear RMS-flux relationship holds for the Comptonised power-law-like component in many accreting systems, from accreting white dwarfs to AGN, suggesting a common physical origin for the broadband intrinsic

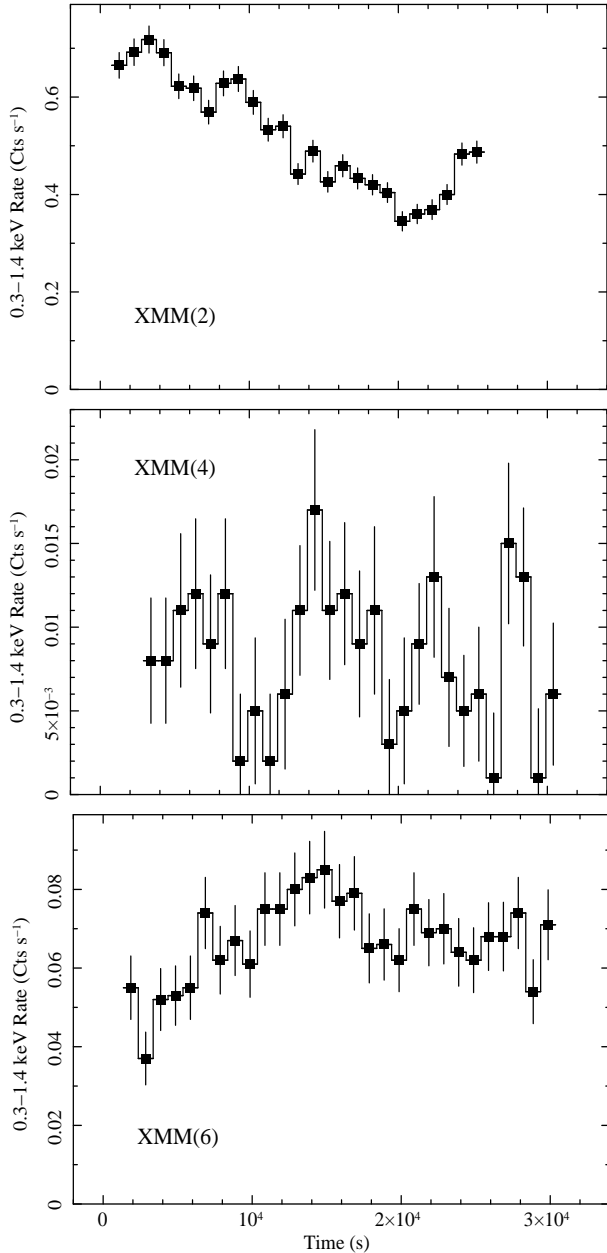


Figure 11. From top to bottom we show the background-subtracted light curve of PHL 1092 from the XMM(2), XMM(4), and XMM(6) observations. The energy band is 0.3–1.43 keV (~ 0.4 –2 keV in the rest frame) and all light curves have 1 ks bin size, corresponding to ~ 715 s in the rest frame.

coronal X-ray variability, independent of source type (e.g. Uttley et al. 2004; Scaringi et al. 2012).

In order to assess whether similar properties are present in PHL 1092, we then compute the RMS variability of PHL 1092 in the frequency range of 0.05 – 1 mHz (0.07 – 1.4 mHz in the rest-frame). The 90% error on the RMS is computed by considering the measurement uncertainty as well as the scatter due to the red component of the noise, using the results in Table 1 of Vaughan et al. (2003) and following the prescriptions of Ponti et al. (2012). The resulting RMS variability as a function of X-ray flux (count rate) is shown in Fig. 12 for all *XMM-Newton* observations. As can be seen, despite the relatively large errors, the RMS variability appears

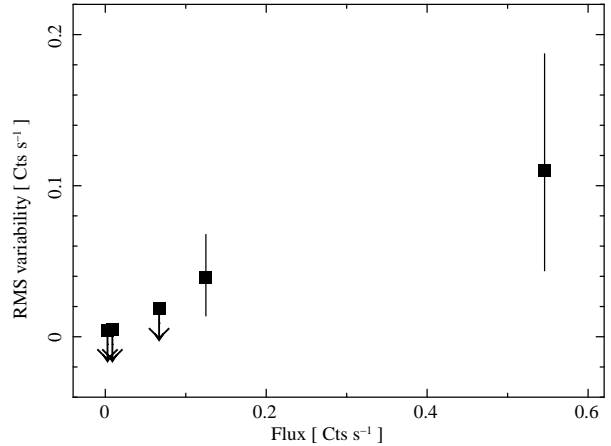


Figure 12. The RMS variability as a function of flux. The RMS variability is computed in the frequency range 0.05 – 1 mHz (0.07 – 1.4 mHz in the rest-frame) for all *XMM-Newton* observations.

to be correlated with flux, in agreement with the expected linear RMS–flux relationship (Uttley & McHardy 2011). The size of the error bars prevents us from claiming a robust linear RMS–flux relationship in PHL 1092, but it is clear, for instance, that the RMS variability of the lowest flux observation ($\text{RMS} \leq 4.2 \times 10^{-3} \text{ Cts s}^{-1}$ for an average count rate of $\sim 2.8 \times 10^{-3} \text{ Cts s}^{-1}$) is at least one order of magnitude smaller than lower possible RMS of the highest flux one⁵ ($\text{RMS} \geq 4.4 \times 10^{-2} \text{ Cts s}^{-1}$ for an average count rate of $\sim 0.55 \text{ Cts s}^{-1}$).

This result indicates that the short- and long-timescale X-ray variability in PHL 1092 are likely to obey the same linear relationship as most other accreting systems. The RMS–flux relationship we tentatively obtain in PHL 1092 may also explain the prolonged low flux state from observations XMM(3) to XMM(4) which are separated by ~ 1 yr in the quasar rest-frame; the low flux state of PHL 1092 can be seen simply as the continuation to long timescales of the non-linear behaviour implied by the RMS–flux relationship. In practice, as the linear RMS–flux relationship implies that the fluxes have a log-normal distribution, AGN with large variability amplitudes (such as PHL 1092) are more likely to exhibit excursions into relatively prolonged low flux states than into high flux ones. This behaviour has indeed been observed in a number of AGN and, especially, in those with large variability amplitudes such as the NLS1 galaxies NGC 4051 and 1H 0707–495 (see examples of prolonged low flux states in Fig. 1 of Vaughan et al. 2011, and Fig. 1 of Fabian et al 2012). The lack of variability during prolonged low-flux states and the extreme variability amplitude during high-flux intervals are just opposite extremes of the linear RMS–flux relationship. As for the frequency with which extreme flux variations can occur, Gibson & Brandt (2012) have shown that extreme X-ray variations ($\geq 100\%$) such as those observed in PHL 1092 are quite rare (an upper limit of about 4% of observations) in quasars with similar optical luminosity.

Our baseline and reflection spectral models are associated with large and moderate intrinsic variability respectively. As such, a RMS–flux linear relationship has to be expected. On the other hand, this is not the case for the absorption model, as most (if not all) of the long-term X-ray variability is attributed to absorption changes. It remains to be seen whether a scenario in which most of

⁵ See Table 2 for c.g.s. fluxes in the 0.5–2 keV band.

the long–timescale flux variability is induced by obscuring structures can naturally reproduce the linear RMS–flux relation we suggest to exist in PHL 1092.

8.1 Long–timescale variability

We now consider the typical rate of change of the physical parameters governing the flux variability of PHL 1092 on long–timescales in the framework of the three scenarios we propose.

8.1.1 Breathing corona (baseline) scenario

The X–ray flux is, in this model, determined by the size of the X–ray corona. As shown in the top panel of Fig. 7, the baseline model suggests a *breathing corona* scenario in which the corona outer boundary R_c changes with time. In order to assess the typical rate of change $\langle \Delta R_c / \Delta T \rangle$, we define ΔR_c as the difference in corona size between two subsequent *XMM–Newton* observations separated by a time span ΔT (in the quasar rest–frame). In the top panel of Fig. 13 we show the resulting $\Delta R_c / \Delta T$ as a function of the rest–frame time–span ΔT for the case of a Schwarzschild BH. The lowest data point at ~ 1 yr (corresponding to the rate of change between the two lowest X–ray flux observations) may be seen as an outlier, especially for the absorption model discussed below. Hence, we define here the typical $\langle \Delta R_c / \Delta T \rangle$ as the average obtained ignoring the lowest data point. We have $\langle \Delta R_c / \Delta T \rangle \sim 1.24 r_g \text{ yr}^{-1}$ which, assuming the BH mass for the Schwarzschild case, corresponds to a radial velocity of $\sim 13.7 \text{ km s}^{-1}$ (we would have $\sim 15.8 \text{ km s}^{-1}$ assuming a Kerr BH instead, again showing the qualitative similarity of the two solutions). This *shrinking velocity* is likely larger than the radial drift in the inner accretion disc (Frank, King & Raine 1985). Hence, the corona outer boundary is unlikely to actually physically shrink. Its apparent motion is most likely related to a change of the active region typical size and location rather than to real motion of the coronal outer boundary. Notice that the lowest data point, corresponding to the $\Delta R_c / \Delta T \sim 0.2 r_g \text{ yr}^{-1}$ between the two lowest X–ray flux observations XMM(3) and XMM(4), is $\sim 6\sigma$ away from the typical rate of change.

8.1.2 Absorption scenario

The covering fraction rate of change $\Delta C_f / \Delta T$ as a function of ΔT is shown in the middle panel of Fig. 13. The horizontal line refers to $\langle \Delta C_f / \Delta T \rangle \sim 0.26 \text{ yr}^{-1}$, obtained by excluding the lowest data point which is a clear outlier at more than 30σ . The presence of such a highly significant outlier means that the low flux states are not only anomalous for their extreme X–ray weakness, but also because the almost complete covering of the X–ray source (i.e. the extreme low flux state) lasts too long with respect to what would be expected based upon the typical covering fraction rate of variation. In summary, the similar and high covering fraction in two observations separated by ~ 1 yr has to be regarded as coincidental, which takes away some of the appeal of the absorption scenario.

8.1.3 Disc–reflection scenario

The disc–reflection flux rate of change $\Delta F_{\text{ref}} / \Delta T$ as a function of ΔT is shown in the bottom panel of Fig. 13, where the reflection flux is computed in the 0.001–300 keV band. The typical reflection flux rate of change is $\langle \Delta F_{\text{ref}} / \Delta T \rangle \sim 2.7 \times$

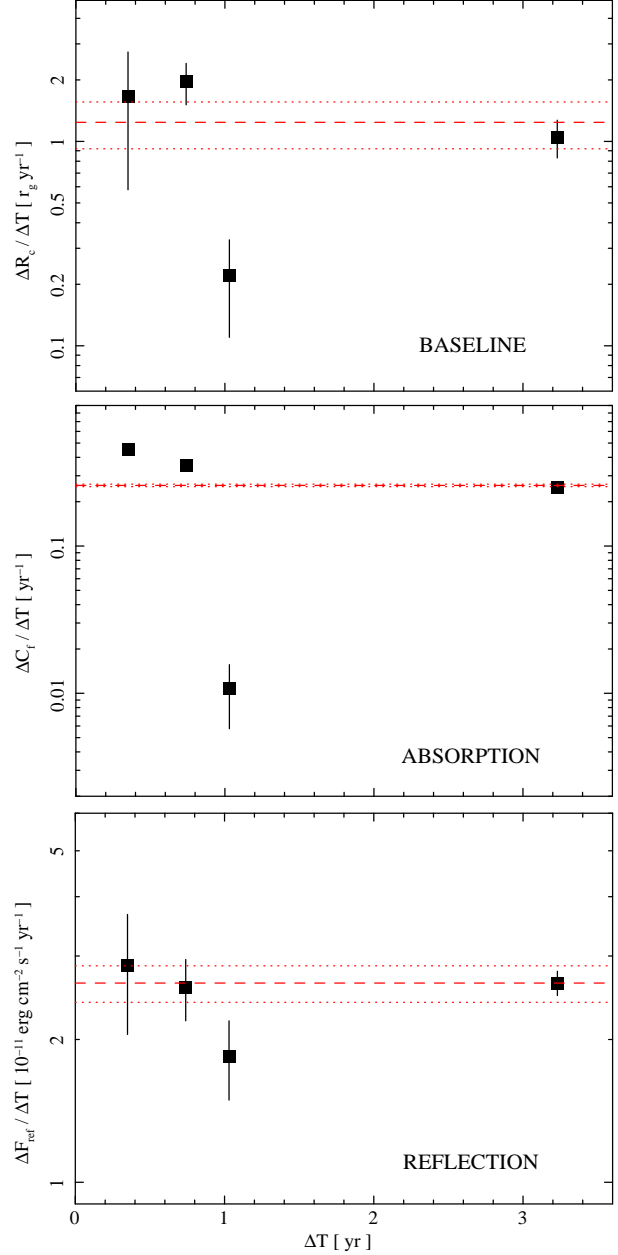


Figure 13. **Top:** The outer corona boundary rate of change according to the baseline *breathing corona* model for the Schwarzschild BH case. We also show the average $\langle \Delta R_c / \Delta T \rangle \sim 1.24 r_g \text{ yr}^{-1}$, which has been obtained by ignoring the lowest data point at ~ 1 yr, together with its 90% error. $\langle \Delta R_c / \Delta T \rangle$ corresponds to a radial velocity of $\sim 13.7 \text{ km s}^{-1}$ for the adopted BH mass. **Middle:** The covering fraction rate of change according to the absorption model. We also show the typical $\langle \Delta C_f / \Delta T \rangle \sim 0.26 \text{ yr}^{-1}$, obtained ignoring the lowest data point. A better fit for the three highest data points can be obtained as $\Delta C_f / \Delta T \propto \Delta T^{-0.24}$ without changing the outlier nature of the lowest data point. **Bottom:** The disc–reflection total flux rate of change according to the disc–reflection model. F_{ref} is proportional to the flux irradiating the disc at all times and, as such, to the disc ionisation. We also show the typical flux rate of change $\langle \Delta F_{\text{ref}} / \Delta T \rangle \sim 2.6 \times 10^{-11} \text{ erg cm}^{-2} \text{ s}^{-1} \text{ yr}^{-1}$, obtained ignoring the lowest data point.

10^{-11} erg cm $^{-2}$ s $^{-1}$ yr $^{-1}$. The flux rate of change between the two lowest X-ray flux observations is only $\sim 2\sigma$ away from the typical rate. Hence, all flux states, including the extremely X-ray weak ones, are consistent with the typical variability of PHL 1092 on long-timescales at the 2σ level.

8.2 Short-timescale variability

We now consider the short-timescale (\sim ks) intra-observation variability of PHL 1092. For simplicity, we focus here on the highest flux XMM(2) observation only, where a smooth decline of soft X-ray flux by a factor ~ 2 in ~ 23 ks (~ 16.5 ks in the rest-frame) is seen (top panel of Fig. 11). This ensures that the most stringent limits based on the short-timescale variability can be derived since, as shown in Fig. 12, the RMS-flux correlation implies that the highest flux observation is also the one with the largest RMS variability.

Let us first consider the excess variance σ_{nxss}^2 as a measure of the X-ray variability in XMM(2). We refer to Ponti et al. (2012) for the operative definition of the excess variance and its error. Using time bins of 250 s and dividing the XMM(2) light curve in intervals of 10 ks (both in the quasar rest frame), we have $\sigma_{\text{nxss},10\text{ks}}^2 = 0.012_{-0.005}^{+0.063}$ in the 0.4–2 keV band (rest-frame). As shown by Ponti et al. (2012), the X-ray excess variance in the soft and hard X-ray band are tightly correlated. If this is the case for PHL 1092 as well, we can then make use of the results in Table 3 of Ponti et al. (2012), where the authors report the $\sigma_{\text{nxss}}^2 - M_{\text{BH},X}$ relationship for the hard X-ray σ_{nxss}^2 , to give an estimate of the BH mass of PHL 1092 as derived from its X-ray variability. We obtain $M_{\text{BH},X} = 6_{-5}^{+10} \times 10^6 M_{\odot}$, in good agreement with previous studies (Nikołajuk, Czerny & Gurynowicz 2009). We point out, however, that this result is obtained assuming that the soft X-ray excess variance is indeed tightly correlated with the hard X-ray one, as the case for the AGN in the work by Ponti et al. (2012). However, the soft X-ray variability in PHL 1092 may not be intrinsic (but driven, for example, by absorption changes) and may thus over-estimate the intrinsic X-ray variability of the source. We should then take a conservative approach and consider the $M_{\text{BH},X}$ value derived above as a lower limit.

As already discussed by Nikołajuk et al. (2009), the BH mass derived from PHL 1092 X-ray-variability is about two orders of magnitude lower than that estimated through single-epoch optical spectra, which is $M_{\text{BH,opt}} \sim 3 \times 10^8 M_{\odot}$. This means that i) the short-timescale variability of PHL 1092 is exceptionally high with respect to the AGN population or ii) the formulae used to derive the BH mass from the optical luminosity and the H β FWHM do not apply as standard in the case of PHL 1092. As a note of caution, it should be mentioned that PHL 1092 is a wind-dominated object in the UV (see Section 4). The standard BH mass scaling relations (e.g. Vestergaard & Peterson 2006) are based on reverberation-mapped objects which are not wind-dominated. Moreover, the H β emission region likely sees a continuum which has been filtered through the wind, which makes the mass scaling relation possibly more uncertain in this case. Hence, the BH mass scaling relations may not be highly reliable for wind-dominated systems such as PHL 1092, as discussed by Richards et al. (2011).

The BH mass derived from our UV-to-X-ray spectral analysis with the baseline model is much higher than that derived from X-ray variability and, in the Kerr BH case, it is also much higher than $M_{\text{BH,opt}}$ (we derive $\sim 2.4 \times 10^8 M_{\odot}$ and $\sim 1.7 \times 10^9 M_{\odot}$ for the Schwarzschild and Kerr BH cases respectively, see Table 3). The BH mass we derive from spectral fitting is based on the assumption that the optical/UV emission detected with the OM is entirely due

to intrinsic accretion disc thermal emission. It is impossible, in fact, to reach the OM fluxes with a lower BH mass and with a reasonable value for the Eddington ratio (say lower than 5), so that the data do not seem to allow for much lower BH masses than those reported in Table 3. The only way to lower the BH mass from spectral fitting would be to consider that the optical/UV fluxes are contaminated or even dominated by a different emission component. Such component may be reprocessed emission, likely a combination of disc thermal reprocessing and reflection, plus scattering from the UV wind. This may be relevant for our reflection-dominated model (which prefers the Kerr solution, hence a likely too large BH mass) for which a significant contribution of reprocessing to the UV flux has to be expected. In summary, if reprocessing is important, the BH mass derived from our spectral fits to the UV and X-ray data is likely over-estimated. However, the lack of a self-consistent disc reprocessing model (thermal plus reflection) from optical/UV to X-rays, and of a reliable model for the wind scattering contribution to the UV continuum, does not allow us to robustly infer reliable BH mass estimates within this scenario.

The short-timescale X-ray variability of PHL 1092 can also be used to constrain the X-ray corona size under the assumption that the variability is intrinsic (if not, the coronal size derived below has to be considered as a lower limit). As can be seen in Fig. 11, significant variability is detected down to the bin size. In fact, considering shorter bins, we detect significant variability down to $\Delta t = 500$ s during the XMM(2) high-flux observation. Simple light-travel time arguments imply an X-ray corona size of the order of $D_c = c\Delta t/(1+z) \sim 1.1 \times 10^{13}$ cm. The gravitational radius scales linearly with the BH mass and is $1.48 M_8 \times 10^{13}$ cm, where M_8 is the BH mass in units of $10^8 M_{\odot}$, so that $D_c \simeq 0.7 r_g M_8^{-1}$. Hence, any BH mass exceeding $1.4 \times 10^8 M_{\odot}$ would imply a very compact corona with $D_c \leq 1 r_g$. Even considering the uncertainty in BH mass discussed above, this result suggests that X-rays come from one single compact active region at any given time, supporting the compact corona required by our reflection-dominated model.

Let us now consider the implications of the short-timescale variability of PHL 1092 for the three proposed scenarios. We assume here that the same mechanism responsible for the long-timescale variability acts also on short-timescales. This is of course a strong assumption, and we cannot exclude that two different processes are at play on different timescales. It is however instructive to explore the consequences of such an assumption on the proposed spectral/variability models.

8.2.1 Breathing corona (baseline) scenario

In the *breathing corona* scenario, the observed XMM(2) short-timescale variability can be produced by a smooth contraction of the corona outer boundary from $R_c \sim 10.3 r_g$ to $\sim 8.9 r_g$ (we discuss the Schwarzschild case only for simplicity). As this happens in 16.5 ks in the rest-frame, the short timescale variability implies an unphysically large radial velocity of $\sim 0.3 c$. This highly relativistic radial velocity of the corona outer boundary reinforces our conclusion that the X-ray corona cannot physically shrink. The measured R_c is much more likely to represent the typical size (and/or distance from the BH) of the X-ray active region at any given time. For example, the rate of change of R_c could represent the velocity with which the magnetic structures responsible for heating the coronal plasma can re-organise themselves, leading to the activation of X-ray emitting regions of different size and/or location.

8.2.2 Absorption scenario

For the absorption model, the observed variability can be obtained with a covering fraction change of $\Delta C_f \sim 50\%$ in $\Delta T \sim 16.5$ ks (rest-frame). Considering an X-ray source size D_s and covering from a single obscuring structure (cloud), this corresponds to a cloud velocity of $v \sim \Delta C_f D_s / \Delta T = (D_s / r_g) \times 1.06 \times 10^9 \text{ cm s}^{-1}$ for our best-fitting BH mass in the Schwarzschild case. Assuming a typical X-ray source size of $10 r_g$, we infer a cloud velocity $v \sim 0.35 c$ in the plane of the sky. This velocity is of the order of the outflow velocity that we infer from our spectral analysis by identifying the ~ 1 keV absorption feature with Fe L absorption. Such an outflow velocity is also in the range of that of the ultra-fast outflows that have been claimed at Fe K energies in a significant fraction of radio-quiet AGN (e.g. Tombesi et al. 2010 and 2012). In summary, if absorption is invoked to explain not only the long-timescale but also the short-timescale variability, a ultra-fast outflow is necessary. Such a high velocity, however, makes it even more difficult to explain the prolonged low flux states of observations XMM(3) and XMM(4) as clouds moving relativistically should cover/uncover the X-ray source on very short-timescales.

8.2.3 Disc-reflection scenario

In the reflection-dominated scenario, the X-ray flux variability is driven by the variability of the flux irradiating the accretion disc together with the associated disc ionisation change. Considering our best-fitting model for observation XMM(2), we find that the observed soft X-ray flux variability is reproduced with a slightly smaller variation of the irradiating flux and ionisation state, namely a factor ~ 1.5 instead than a factor 2 in 16.5 ks (rest-frame). This corresponds to $\Delta F_{\text{ref}} / \Delta T \sim 2 \times 10^{-15} \text{ erg cm}^{-2} \text{ s}^{-2}$. The reduction of the intrinsic X-ray variability amplitude because of ionisation effects also reduces the intrinsic excess variance by $\sim 50\%$, and slightly increase the X-ray variability BH mass estimate which, according to this model, would be of the order of $M_{\text{BH,X}} \sim 10^7 M_{\odot}$ (although with large errors).

9 SUMMARY OF THE DATA ANALYSIS RESULTS

We have applied to our *XMM-Newton* monitoring observations of PHL 1092 a series of models that can explain the extreme X-ray (α_{ox}) variability of PHL 1092 within different contexts. Below, we summarise the results of our analysis in the framework of the three proposed scenarios.

9.1 Baseline model

Our baseline model implies an intrinsic X-ray flux variation of more than two orders of magnitude in 3.2 yr (rest-frame). Within the framework of that model, this flux variation is associated with the collapse of an already compact X-ray corona down to the ISCO (or close to it). This result is obviously highly model-dependent as by construction the only way in which the model can produce variable X-ray output at fixed Eddington ratio is by varying the X-ray corona size. Any model able to account for large X-ray variability and almost constant optical/UV emission would be successful. However, the model is reasonably self-consistent and provides an elegant solution in terms of a breathing X-ray corona for α_{ox} variation that is entirely driven by X-ray flux variability, as is the case in PHL 1092 (see Fig. 2). The model accounts for the soft excess

in terms of Comptonization of the soft disc photons in the optically thick corona. Its electron temperature is similar to that inferred from the analysis of the soft excess in the vast majority of type 1 AGN. As such, it remains to be seen whether this remarkably uniform electron temperature in accreting BH spanning orders of magnitude in BH mass and Eddington ratio can be physically explained.

In both the Schwarzschild and Kerr cases, the observed ΔR_c implies a radial shrinking of the X-ray corona outer radius with a radial velocity of $\sim 10 - 15 \text{ km s}^{-1}$, increasing to $\sim 0.3 c$ if the model also needs to explain the short-timescale X-ray variability of PHL 1092. This suggests that the corona is not actually physically shrinking, but that the heating mechanism (likely associated with magnetic fields) is occurring in more localised sites during low-flux states. Notice that the very compact X-ray corona in low-flux states would also imply that light-bending effects can no longer be neglected, likely producing a strong reflection contribution off the inner accretion disc. As such, the model is not entirely self-consistent. However, the relatively limited quality of the data does not allow us to include the disc reflection component into the baseline model without over-modelling the X-ray data.

9.2 Absorption model

The absorption model is based on the idea that the observed dramatic X-ray flux variability is not intrinsic but is due to intervening absorption. Indeed, we find an attractive solution in which the intrinsic X-ray flux of PHL 1092 is constant as is the UV flux (and hence the accretion rate). The observed variability can be entirely explained in terms of a relatively cold absorber (with $\log \xi \leq -1.0$) with varying covering fraction. The absorber covers $\sim 19\%$ of the X-ray corona in high X-ray flux states and almost 100% of it in low flux ones. It should be pointed out that such a low-ionization absorber should imprint absorption features in the UV, which are not seen in the HST spectrum. This issue will be discussed in Section 10. Remarkably, the intrinsic (constant) X-ray flux of PHL 1092 in the absorption scenario is consistent with that expected for a quasar with the PHL 1092 optical luminosity. Hence, within the absorption-dominated scenario, PHL 1092 is an intrinsically standard quasar with $\Delta \alpha_{\text{ox}} \sim 0$. An absorption feature at ~ 1.5 keV in the rest-frame is also seen and cannot be produced by the relatively low-ionisation absorber. If the feature is identified with the Fe L complex, it implies the presence of a second absorbing phase with relatively high-ionisation and highly relativistic outflow velocity (of the order of $\sim 0.3 c$).

Such a highly relativistic outflow velocity may be shared by the cold absorber as well. In fact, if we make the strong requirement that the model must be able to reproduce also the short-timescale X-ray variability of PHL 1092 with covering fraction changes, a similar outflow velocity must be invoked for the cold absorber as well. On the other hand, such velocity makes it difficult to account naturally for the fact that the two subsequent observations XMM(3) and XMM(4), separated by ~ 1 yr in the rest-frame, share an almost identical covering fraction (of $\sim 100\%$). This prolonged low flux state is at odds with the typical absorber variability properties which would predict a $\Delta C_f \sim 0.2 - 0.3$ over a ~ 1 yr timescale.

In summary, the absorption model can explain the variability of PHL 1092 on long-timescales but requires the extremely X-ray weak states to be somewhat exceptional as they are clear outliers and do not match the typical absorption variability properties on long-timescales. The bottom line is that the low flux states last too long to match the typical covering fraction rate of change. In fact,

excursions into relatively prolonged low flux states are a common characteristic of AGN with large variability amplitude and obeying a linear RMS–flux relationship, which we suggest exists in PHL 1092 as well. It remains to be seen whether a self-consistent absorption model is able to induce a linear RMS–flux relationship, thus explaining the prolonged low flux states in the absorption scenario. On the other hand, the baseline and reflection models, which are both associated with intrinsic X-ray flux variability, are naturally coupled to the linear RMS–flux relationship (which predicts prolonged low–flux states), so that they may be regarded as less problematic in this respect.

9.3 Reflection model

A reflection-dominated model represents a plausible alternative to the scenarios discussed above. We are able to reproduce the observed factor ~ 260 variation at 2 keV by only invoking a factor ~ 10 change in the intrinsic X-ray flux, coupled with associated disc ionisation changes. The excellent correlation between the disc ionisation and the total reflection flux (proportional to that irradiating the disc) ensures that the model is self-consistent. Ionised disc reflection also provides a natural explanation for the soft X-ray excess with no need for Comptonization in an optically thick corona, which is not the case for any of the above models. The model implies that PHL 1092 appears predominantly X-ray weak because its X-ray corona is extremely compact and centrally concentrated, within a few r_g from the BH. Such compact corona also self-consistently predicts reflection-dominated spectra because of light-bending effects. In absence of light-bending, PHL 1092 would in fact appear as a non-X-ray weak quasar with a residual α_{ox} variation due to moderate intrinsic X-ray variability (a factor 10 in 3.2 yr in the rest-frame).

The reflection model can explain both the long- and short-timescale X-ray variability of PHL 1092 with relatively modest intrinsic flux changes. As the model is associated with intrinsic variability, the (tentative) linear RMS–flux relationship we suggest to exist in PHL 1092 comes as no surprise. Hence the relatively prolonged low–flux state (lasting ~ 1 yr) can be seen simply as a consequence of the RMS–flux linear relationship (i.e. of the log-normal distribution of fluxes).

10 DISCUSSION: PHL 1092 IN THE WIDER CONTEXT

PHL 1092 shares many common properties in the optical/UV with the prototypical non-BAL X-ray weak quasar PHL 1811 (see also the case of LBQS 0102-2713, Boller, Schady & Heftrich 2011). Their UV spectra are characterised by weak, broad, and asymmetric high-ionisation emission lines and strong, narrow, low-ionisation lines at the rest-frame wavelength. Most of their unusual optical/UV properties can be understood by assuming a two-component broad-emission-line-region (BELR) comprising a wind (e.g. C IV) and a disc (e.g. Mg II) component irradiated by a soft SED depleted of X-ray photons (Leighly et al. 2007b; Wu et al. 2011). Filtering of the ionising flux through the wind also explains the lack of high-ionisation lines in the disc component which is then located at a greater distance from the BH than the wind launching site. The implication is that the BELR sees a soft X-ray weak SED which may be intrinsic to these sources (as in our baseline model), due to absorption, or induced by light-bending effects.

Our baseline model associates X-ray weak sources with a

compact corona confined within a few r_g from the BH. This result arises because the X-ray output is proportional to the size of the X-ray corona, i.e. $L_X \propto (1 - R_c/R_{\text{isco}})$. In this respect, the baseline model resembles the disc-reflection one, as the X-ray emission from an extremely compact corona will inevitably be affected by light-bending effects, which further reduce the X-ray output at infinity and imply the presence of reflection-dominated spectra, especially if a rapidly rotating Kerr BH is considered. We are therefore left with two main physical scenarios: PHL 1092 (and likely other non-BAL X-ray weak sources) is characterised by i) an unusually compact X-ray corona or ii) X-ray-only absorption.

Wu et al. (2011) recently collected a sample of 10 PHL 1811 analogs at high redshift with a mean $\Delta\alpha_{\text{ox}} \sim -0.40$. The X-ray analysis of this sample suggests that these objects have an average photon index $\Gamma = 1.2 \pm 0.5$, which appears to be harder than that of standard X-ray detected AGN, although the relatively large error bar does not allow firm constraints on the spectral shape. If the typical spectrum of the PHL 1811 analogs is indeed harder than usual, it may be related either to intervening absorption or to the presence of a reflection-dominated spectrum, two of the models that we consider here for PHL 1092 and that have been suggested by Wu et al. (2011) for the PHL 1811 high-redshift analogs.

If absorption is invoked, the material must lie closer to the central BH than the BELR (say that for Mg II) so that the ionising continuum is effectively X-ray weak thus explaining the observed optical/UV emission line properties (see Leighly 2004). On the other hand, UV disc photons should not be affected, as no absorption is seen in the UV spectrum. The X-ray absorber could be naturally associated with the putative shield which is often invoked in outflow models not to over-ionise the gas at the base of the outflow, thus enabling acceleration (e.g. Murray et al. 1995; Wu et al. 2011). As such, the absorber may be co-spatial with the outflow: wind simulations show that the outflow is likely self-shielding as the column density close to the disc surface can be high enough to enable the acceleration of a line driven wind (e.g. Proga, Stone & Kallman 2000; Proga & Kallman 2004). This shielding X-ray absorber could well have been detected in a few cases of BAL quasars (e.g. Chartas et al. 2002). If low-ionisation high-column-density gas exists at almost all radii close to the disc surface (as per e.g. Proga & Kallman 2004, see their Fig. 1), the UV emission from the extended disc would always be affected, independently of the specific line-of-sight. Hence, such simulations may not be totally relevant for the case of AGN with no absorption signatures in the UV.

The lack of UV absorption in PHL 1092 (and the presence of the broad, blueshifted C IV emission line) most likely indicates that our line-of-sight only crosses the highly-ionised outflow polar zones, so that no absorption features are imprinted in the UV. According to the work of Schurch, Done & Proga (2009), which is based on the wind simulations by Proga & Kallman (2004), polar lines-of-sight are characterised by high ionisation, while equatorial ones by cold absorption (i.e. equatorial lines-of-sight intercept the gas responsible for the shielding). A pole-on line-of-sight into the wind funnel would indeed be consistent with the detected blueshifted C IV emission line.

Let us now consider whether the X-ray-only absorber we infer from our absorption-model is consistent with this picture. The flux variability and transient X-ray weakness of PHL 1092 is due to the variation of the covering fraction of a relatively cold absorber with $\log \xi \leq -1.0$. If the absorber also covers the UV-emitting disc, such a low-ionisation absorber would imprint features in the UV spectrum as well, as seen in BAL quasars but not in PHL 1092

and similar sources. Indeed, according to Proga & Kallman (2004), such low-ionisation is only achieved for equatorial lines-of-sight (say $\geq 70^\circ$, see Fig. 1 of their work). This means that we would be intercepting the denser part of the outflow (basically the shielding gas), which conflicts with the fact that no absorption features are imprinted in the UV (dominated instead by broad and blueshifted emission lines).

The presence of a cold X-ray absorber associated with the lack of UV absorption represents a problem for the absorption scenario, as detailed by Wu et al. (2011). The only possible way out we can envisage is that the X-ray absorber is more compact than the UV-emitting disc so that the UV emission is not significantly absorbed. Let us assume an absorber confined within a fiducial radius of $\sim 50 r_g$, so that the UV emission from within that region is small and the UV spectrum does not present any absorption feature. Our absorption model is based on the XSTAR code, and the ionisation parameter is defined as $\xi = L_{\text{ion}}/(R^2 n)$, where n is the gas number density, R its distance from the ionising source, and L_{ion} the ionising luminosity between 1 and 1000 Ry. The intrinsic ionising luminosity of PHL 1092 is $L_{\text{ion}} \sim 3.5 \times 10^{46} \text{ erg s}^{-1}$, so that $n(R/r_g)^2 = 2.9 \times 10^{19} \xi^{-1} \text{ cm}^{-3}$ (adopting the best-fitting BH mass in the Schwarzschild case). For the ionisation parameter we derive ($\log \xi \leq -1.0$), this implies that a compact absorber with $R \sim 50 r_g$ can only be obtained with $n \geq 10^{17} \text{ cm}^{-3}$, which seems highly unlikely.

Hence the absorption model we propose is not self-consistent as the low-ionisation gas detected in absorption (and needed to reproduce the X-ray flux variability) cannot survive in the compact region that is necessary to avoid significantly affecting the UV. This conclusion is, however, somewhat model-dependent because our absorption model is likely over-simplified. For instance, one can imagine a situation in which the absorbing cloud(s) have a multi-layer structure. The outer layers are highly ionised and reduce via absorption and Compton scattering, the ionising luminosity irradiating the inner layers. If so, the cloud(s) core could possibly survive with relatively low ionisation even very close to the ionising source. This hypothesis would require consideration of a multi-layer absorption model in which Compton scattering is self-consistently taken into account, which also means considering with care all possible outflow geometries/velocities. Given the limited quality of our X-ray data, we must defer this study to future higher quality observations of PHL 1092 or of other similar (X-ray brighter) sources.

If a reflection-dominated spectrum is invoked, the overall optical/UV to X-ray SED is intrinsically steep as the ionising continuum is X-ray depleted and, as such, the unusual optical/UV emission line properties of PHL 1092 and other similar sources can be explained. We attribute this effect to light-bending close to the BH which depresses very significantly the continuum flux that can escape to an observer at infinity. Our analysis of PHL 1092 shows that a reflection-dominated spectrum due to the presence of a very compact and centrally concentrated X-ray corona (few r_g in size) can indeed produce extreme X-ray weak states as well as dramatic X-ray variability in the soft band by invoking much lower amplitude variation in the intrinsic X-ray flux. Most of the soft X-ray variability is accounted for by moderate disc ionisation variation, associated with the similar amplitude intrinsic flux.

As mentioned above, the UV properties of PHL 1092 are similar to those of two other X-ray weak NLS1 galaxies: 1H 0707–495 and IRAS 13224–3809. Remarkably, the X-ray spectra of 1H 0707–495 and IRAS 13224–3809 have been interpreted as being disc-reflection-dominated (Boller et al. 1993, 2002, 2003; Fabian et al. 2002, 2004, 2009, 2012; Ponti et al. 2010). In both

cases, a significantly enhanced Fe abundance is required to model the X-ray spectrum which is in agreement with the enhanced metallicity inferred by Leighly (2004b) from the UV spectra. A recent observation of 1H 0707–495 (Fabian et al. 2012) suggests that the X-ray corona is confined within $\sim 2 r_g$ from the central BH during extremely low X-ray flux states, while it is likely more extended during higher X-ray flux states, in agreement with light-bending model predictions (Miniutti & Fabian 2004). Moreover, soft X-ray time lags of the order of the light-crossing time of a few r_g have been detected in 1H 0707–495, and their properties (energy and frequency dependence) support the overall interpretation in terms of disc reflection (Fabian et al. 2009; Zoghbi et al. 2010; Zoghbi, Uttley & Fabian et al. 2011). It should be mentioned that, although no complete spectral-timing model has been presented, the properties of 1H 0707–495 have been suggested to be consistent with an absorption-dominated interpretation, which, however, may require a special line-of-sight (Miller et al. 2010). The detection of time-lags in several other sources appears to exclude the possibility that we are dealing with such special lines-of-sight (e.g. Emmanoulopoulos, McHardy & Papadakis 2011; Tripathi et al. 2011; Zoghbi & Fabian 2011; Zoghbi et al. 2012). Moreover, the time-lag amplitude appears to scale with BH mass as predicted within the reverberation scenario if the reflector is few r_g only from the X-ray source (De Marco et al. 2012). Gibson, Brandt & Schneider (2008) showed that non-BAL X-ray weak quasars make up less than about 1–2% of the optically selected quasar population. On the other hand, Wu et al. (2011) reported that the fraction of PHL 1811 analogs in the radio-quiet population is $\leq 1.2\%$. It is reassuring that the fraction of AGN that can be very strongly reflection-dominated is constrained to be $\leq 2\%$ by the hard X-ray cosmic background (Gandhi et al. 2007), although the cosmic X-ray background sources are likely in a different luminosity regime from the SDSS quasars considered by e.g. Wu et al. (2011).

11 CONCLUSIONS

We have analysed *XMM-Newton* observations of PHL 1092 covering nearly 10 yr (7.5 yr in the rest-frame) of its activity and spanning more than two orders of magnitude in soft X-ray flux. We complement our analysis with optical spectra obtained in January 2008 and October 2010 and with a qualitative discussion of the UV HST spectrum from a August/September 2003 STIS observation. The main results of our analysis can be summarised as follows:

(i) The remarkable α_{ox} variability of PHL 1092 is entirely driven by the X-ray variability. During our monitoring campaign, we detect a maximum X-ray flux variability by a factor ~ 260 in ~ 3.5 yr (rest-frame), while the UV variability is confined to within 10–15%. At its minimum X-ray flux level (January 2008), PHL 1092 is about a factor of ~ 480 X-ray weak with respect to a standard quasar with its optical luminosity.

(ii) The UV spectrum of PHL 1092 is characterised by weak, broad, and blueshifted C IV emission, most likely originating in a wind. The lack of absorption features in the UV spectrum of PHL 1092 most likely indicates that the outflow does not cross our line-of-sight, in contrast with the case of BAL quasars. It presents many analogies with the prototypical non-BAL X-ray weak quasar PHL 1811 and with the two NLS 1 galaxies 1H 0707–495 and IRAS 13224–3809. We tentatively report UV variability in the C IV region based on a comparison between the single-epoch HST spectrum and the UV photometry from the *XMM-Newton* OM observations. The possible C IV variability appears to be associated with

X-ray weakness. Our results are consistent with the idea that the C IV emission line is weaker and/or more blueshifted in X-ray weaker states. This implies either that the ionising flux drop associated with X-ray weak states is sufficient to depress the C IV emission-line flux, or that the outflow can be launched from closer in during X-ray weak states, thus resulting in a larger outflow velocity and C IV blueshift. The optical spectrum of PHL 1092 is dominated by Fe II, and is characterised by relatively narrow H β and Mg II lines centred at rest-frame energies, likely originating in the dense outer disc. No significant spectral changes are seen in the optical from 2008 to 2010.

(iii) The X-ray variability of PHL 1092 on long- and short-timescales suggests a correlation between the X-ray flux and the RMS variability, consistent with the linear RMS-flux relationship that has been now observed in almost all types of accreting objects. PHL 1092 has a high variability amplitude on short-timescales which can be used to estimate its BH mass. The X-ray variability BH mass estimate is, however, about two orders of magnitude smaller than that obtained using the standard BH mass scaling relations using single-epoch optical spectra. This result calls into question either the idea that the mechanism behind the short-timescale variability of PHL 1092 is the same as in all other accreting objects (which would be surprising, given the RMS-flux relation we suggest) or the reliability of the standard mass scaling relations for wind-dominated *soft-spectrum* AGN such as PHL 1092.

(iv) We propose three possible scenarios that can explain the UV-to-X-ray SED of PHL 1092 at all X-ray flux levels: i) a *breathing corona* scenario in which the X-ray flux is correlated with the X-ray corona size and where X-ray weak states are associated with the collapse of the corona down to the marginal stable orbit; ii) an absorption model where the X-ray variability is dominated by changes of the covering fraction of a relatively cold absorber which covers almost 100% of the X-ray source in X-ray weak states; iii) a disc-reflection-dominated scenario where the X-ray corona is confined within few r_g from the central BH at all flux levels.

In the *breathing corona* scenario, the X-ray corona of PHL 1092 is always compact ($\leq 2 R_{\text{isco}}$) and shrinks down to $\sim R_{\text{isco}}$ in extreme X-ray weak states. However, the shrinking radial velocity is likely too high to be plausible and, as such, we interpret the *breathing corona* as an indication that the X-ray active regions are more compact (and likely closer in) in low X-ray flux states. If so, we caution that light-bending effects will inevitably occur, so that the model reduces to the reflection-dominated one at least in extreme X-ray weak states.

The absorption interpretation is not completely self-consistent as the X-ray flux variability is produced by variations of a relatively cold absorber. The absorber should imprint some absorption feature in the UV, but UV absorption is not detected in the spectra of PHL 1092, PHL 1811, the PHL 1811 analogs of Wu et al. (2011), or the two NLS 1 galaxies we consider. One possibility is that the absorber is confined within the UV-emitting disc, i.e. within a few tens of r_g . If so, however, absorbing clouds cannot survive at the low ionisation level we need to reproduce the X-ray variability. A possible way out would be to consider a multi-layer absorption model in which every absorbing cloud is structured into multiple layers. The outer layers may protect the innermost cloud(s) nucleus from the ionising flux, thus enabling them to survive close to the source at low ionisation. We defer such complex study to future work.

As mentioned, the X-ray variability and overall SED can also be reproduced in a reflection-dominated scenario where a compact X-ray corona is confined within few r_g from the BH at all flux levels. Light-bending effects produce a disc reflection-dominated spectrum, and the observed extreme X-ray flux variability at soft X-rays (a factor 260 in 3.5 yr) is reproduced with a much smaller factor of ~ 10 intrinsic variation. A similar scenario has been invoked for 1H 0707-495 and IRAS 13224-3809, two NLS 1 galaxies which share many properties with PHL 1092 from UV to X-rays. The recent detection of soft X-ray time lags in 1H 0707-495 (and other sources) supports a reflection scenario in these objects.

Two of the the three scenarios we present make very different predictions for the X-ray flux above 10 keV. The absorption model implies a constant flux $F_{30-100} \sim 2.5 \times 10^{-13} \text{ erg cm}^{-2} \text{ s}^{-1}$ in the 30-100 keV band, while the reflection-dominated model predicts a much lower flux⁶ of $F_{30-100} \leq 4.1 \times 10^{-14} \text{ erg cm}^{-2} \text{ s}^{-1}$. On the other hand, as the baseline model is associated with very large intrinsic variability, the predicted hard X-ray flux is too variable to provide a useful constraint. A deep observation of PHL 1092 (or of a similar source) with sensitive hard X-ray detectors such as *ASTRO-H* (Takahashi et al. 2010) and *NuSTAR* (Harrison et al. 2010) in the near future may thus reveal the nature of the transient X-ray weakness phenomenon, and could shed light into the nature of the non-BAL X-ray weak quasars population at large.

ACKNOWLEDGEMENTS

Based on observations obtained with XMM-Newton, an ESA science mission with instruments and contributions directly funded by ESA Member States and NASA. We used observations made with the NASA/ESA Hubble Space Telescope, obtained from the Data Archive at the Space Telescope Science Institute, which is operated by the Association of Universities for Research in Astronomy, Inc., under NASA contract NAS 5-26555. The Hobby-Eberly Telescope (HET) is a joint project of the University of Texas at Austin, the Pennsylvania State University, Stanford University, Ludwig-Maximilians-Universität München, and Georg-August-Universität Göttingen. The HET is named in honor of its principal benefactors, William P. Hobby and Robert E. Eberly. The Marcario Low-Resolution Spectrograph is named for Mike Marcario of High Lonesome Optics, who fabricated several optics for the instrument but died before its completion; it is a joint project of the Hobby-Eberly Telescope partnership and the Instituto de Astronomía de la Universidad Nacional Autónoma de México. Funding for the SDSS and SDSS-II has been provided by the Alfred P. Sloan Foundation, the Participating Institutions, the National Science Foundation, the U.S. Department of Energy, the National Aeronautics and Space Administration, the Japanese Monbukagakusho, the Max Planck Society, and the Higher Education Funding Council for England. The SDSS Web site is <http://www.sdss.org/>. GM thanks the Spanish Ministerio de Ciencia e Innovación and CSIC for support through a Ramón y Cajal contract. Financial support for this work was also provided by the Spanish Ministry of Science and Innovation through grant AYA2010-21490-C02-02. GM also thanks CSIC grant PA1003039 and the IoA visitor program for support during an extended Summer visit in Cambridge. WNB thanks NASA ADP grant NNX11AJ59G and NASA grant NNX09AP83G

⁶ We use as upper limit the hard X-ray flux predicted by the highest flux observation model, which is close to the historical highest X-ray flux of PHL 1092, see Fig. 1.

for support. ACF thanks the Royal Society for support. GM wishes to thank Fabrizio Nicastro and Enrico Piconcelli for useful discussions.

REFERENCES

- Behar, E., Sako, M., & Kahn, S. M. 2001, *ApJ*, 563, 497
- Bergeron J., & Kunth D. 1980, *A&A*, 85, L11
- Bergeron J., & Kunth D. 1984, *MNRAS*, 207, 263
- Bessell, M. S. 1991, *A&A*, 242, L17
- Boller, T., Truemper, J., Molendi, S., et al. 1993, *A&A*, 279, 53
- Boller, T., Fabian, A. C., Sunyaev, R., et al. 2002, *MNRAS*, 329, L1
- Boller, T., Tanaka, Y., Fabian, A., et al. 2003, *MNRAS*, 343, L89
- Boller, T., Schady, P., & Heftrich, T. 2011, *ApJ*, 731, L16
- Brandt W.N., Boller Th., Fabian A.C., Ruzskowski M., 1999, *MNRAS*, 303, L53
- Brandt, W. N., Laor, A., & Wills, B. J. 2000, *ApJ*, 528, 637
- Brinkmann, W., Wang, T., Matsuoka, M., & Yuan, W. 1999, *A&A*, 345, 4
- Chartas, G., Brandt, W. N., Gallagher, S. C., & Garmire, G. P. 2002, *ApJ*, 579, 169
- Chartas, G., Brandt, W. N., Gallagher, S. C., & Proga, D. 2007, *AJ*, 133, 1849
- Chartas, G., Saez, C., Brandt, W. N., Giustini, M., & Garmire, G. P. 2009, *ApJ*, 706, 644
- Czerny, B., Nikolajuk, M., Róžańska, A., et al. 2003, *A&A*, 412, 317
- Dasgupta S., Rao A. R., Dewangan G. C. 2004, *ApJ*, 614, 626
- De Marco, B., Ponti, G., Cappi, M., et al. 2011, submitted to *MNRAS* (preprint: arXiv:1201.0196)
- Done, C., Davis, S. W., Jin, C., Blaes, O., & Ward, M. 2012, *MNRAS*, 420, 1848
- Emmanoulopoulos, D., McHardy, I. M., & Papadakis, I. E. 2011, *MNRAS*, 416, L94
- Fabian, A. C., Rees, M. J., Stella, L., & White, N. E. 1989, *MNRAS*, 238, 729
- Fabian, A. C., Ballantyne, D. R., Merloni, A., et al. 2002, *MNRAS*, 331, L35
- Fabian, A. C., Miniutti, G., Gallo, L., et al. 2004, *MNRAS*, 353, 1071
- Fabian, A. C., Zoghbi, A., Ross, R. R., et al. 2009, *Nature*, 459, 540
- Fabian, A. C., Zoghbi, A., Wilkins, D., et al. 2012, *MNRAS*, 419, 116
- Forster, K., & Halpern, J. P. 1996, *ApJ*, 468, 565
- Frank, J., King, A. R., & Raine, D. J. 1985, *Cambridge and New York, Cambridge University Press*, 1985, 283 p.
- Fukugita, M., Ichikawa, T., Gunn, J. E., et al. 1996, *AJ*, 111, 1748
- Gallagher, S. C., Brandt, W. N., Laor, A., et al. 2001, *ApJ*, 546, 795
- Gallagher, S. C., Brandt, W. N., Wills, B. J., et al. 2004, *ApJ*, 603, 425
- Gallo, L. C., Boller, T., Brandt, W. N., Fabian, A. C., & Grupe, D. 2004, *MNRAS*, 352, 744
- Gandhi, P., Fabian, A. C., Suebawong, T., et al. 2007, *MNRAS*, 382, 1005
- Gibson R. R., Brandt W. N., Schneider D. P. 2008, *ApJ*, 685, 773
- Gibson, R. R., & Brandt, W. N. 2012, *ApJ*, 746, 54
- Gierliński, M., & Done, C. 2004, *MNRAS*, 349, L7
- Harrison, F. A., Boggs, S., Christensen, F., et al. 2010, *Proc. SPIE*, 7732, 77320S
- Hill, G. J., Nicklas, H. E., MacQueen, P. J., et al. 1998, *Proc. SPIE*, 3355, 433
- Kalberla, P. M. W., Burton, W. B., Hartmann, D., et al. 2005, *A&A*, 440, 775
- Kwan J., Cheng F.-Z., Fang L.-Z., Zheng W., Ge J. 1995, *ApJ*, 440, 628
- Kruczek, N. E., Richards, G. T., Gallagher, S. C., et al. 2011, *AJ*, 142, 130
- Jin, C., Ward, M., Done, C., & Gelbord, J. 2012, *MNRAS*, 420, 1825
- Just, D. W., Brandt, W. N., Shemmer, O., et al. 2007, *ApJ*, 665, 1004
- Laor, A. 1991, *ApJ*, 376, 90
- Lawrence, A., Elvis, M., Wilkes, B. J., McHardy, I., & Brandt, N. 1997, *MNRAS*, 285, 879
- Leighly K. M. 1999a, *ApJS*, 125, 297
- Leighly K. M. 1999b, *ApJS*, 125, 317
- Leighly, K. M., Halpern, J. P., Helfand, D. J., Becker, R. H., & Impey, C. D. 2001, *AJ*, 121, 2889
- Leighly, K. M., & Moore, J. R. 2004, *ApJ*, 611, 107
- Leighly, K. M. 2004, *ApJ*, 611, 125
- Leighly, K. M., Halpern, J. P., Jenkins, E. B., et al. 2007, *ApJ*, 663, 103
- Leighly, K. M., Halpern, J. P., Jenkins, E. B., & Casebeer, D. 2007, *ApJS*, 173, 1
- Martocchia, A., Karas, V., & Matt, G. 2000, *MNRAS*, 312, 817
- Mathur, S., Matt, G., Green, P. J., Elvis, M., & Singh, K. P. 2001, *ApJ*, 551, L13
- Miller, L., Turner, T. J., Reeves, J. N., & Braitto, V. 2010, *MNRAS*, 408, 1928
- Miniutti, G., Fabian, A. C., Goyder, R., & Lasenby, A. N. 2003, *MNRAS*, 344, L22
- Miniutti, G., & Fabian, A. C. 2004, *MNRAS*, 349, 1435
- Miniutti, G., Ponti, G., Greene, J. E., et al. 2009a, *MNRAS*, 394, 443
- Miniutti, G., Fabian, A. C., Brandt, W. N., Gallo, L. C., & Boller, T. 2009b, *MNRAS*, 396, L85
- Mitsuda, K., Inoue, H., Koyama, K., et al. 1984, *PASJ*, 36, 741
- Murray, N., Chiang, J., Grossman, S. A., & Voit, G. M. 1995, *ApJ*, 451, 498
- Nicastro, F., Fiore, F., & Matt, G. 1999, *ApJ*, 517, 108
- Nikolajuk, M., Czerny, B., & Gurynowicz, P. 2009, *MNRAS*, 394, 2141
- Osterbrock D. E., Pogge R. W. 1985, *ApJ*, 297, 166
- Ponti, G., Miniutti, G., Cappi, M., et al. 2006, *MNRAS*, 368, 903
- Ponti, G., Gallo, L. C., Fabian, A. C., et al. 2010, *MNRAS*, 406, 2591
- Ponti, G., Papadakis, I., Bianchi, S., et al. 2012, *A&A*, 542, A83
- Proga, D., Stone, J. M., & Kallman, T. R. 2000, *ApJ*, 543, 686
- Proga, D., & Kallman, T. R. 2004, *ApJ*, 616, 688
- Ramsey, L. W., Adams, M. T., Barnes, T. G., et al. 1998, *Proc. SPIE*, 3352, 34
- Reeves, J., Done, C., Pounds, K., et al. 2008, *MNRAS*, 385, L108
- Richards, G. T., Kruczek, N. E., Gallagher, S. C., et al. 2011, *AJ*, 141, 167
- Saez, C., Chartas, G., & Brandt, W. N. 2009, *ApJ*, 697, 194
- Scaringi, S., Körtling, E., Uttley, P., et al. 2012, *MNRAS*, 421, 2854
- Schurch, N. J., Done, C., & Proga, D. 2009, *ApJ*, 694, 1

- Shetrone, M., Cornell, M. E., Fowler, J. R., et al. 2007, Proc. of the Astronomical Society of the Pacific, 119, 556
- Strüder, L., Briel, U., Dennerl, K., et al. 2001, A&A, 365, L18
- Takahashi, T., Mitsuda, K., Kelley, R., et al. 2010, Proc. SPIE, 7732, 77320Z
- Telfer, R. C., Zheng, W., Kriss, G. A., & Davidsen, A. F. 2002, ApJ, 565, 773
- Tombesi, F., Cappi, M., Reeves, J. N., et al. 2010, A&A, 521, A57
- Tombesi, F., Cappi, M., Reeves, J. N., & Braitto, V. 2012, MNRAS, 422, L1
- Tripathi, S., Misra, R., Dewangan, G., & Rastogi, S. 2011, ApJ, 736, L37
- Turner, M. J. L., Abbey, A., Arnaud, M., et al. 2001, A&A, 365, L27
- Uttley, P., & McHardy, I. M. 2001, MNRAS, 323, L26
- Uttley, P. 2004, MNRAS, 347, L61
- Uttley, P., McHardy, I. M., & Vaughan, S. 2005, MNRAS, 359, 345
- Vaughan, S., Edelson, R., Warwick, R. S., & Uttley, P. 2003, MNRAS, 345, 1271
- Vaughan, S., Uttley, P., Pounds, K. A., Nandra, K., & Strohmayer, T. E. 2011, MNRAS, 413, 2489
- Vestergaard, M., & Peterson, B. M. 2006, ApJ, 641, 689
- Wang, T. G., Wang, J. X., Brinkmann, W., & Matsuoka, M. 1999, ApJ, 519, L35
- Wilkes B. J., Tananbaum H., Worrall D. M., Avni Y., Oey M. S., Flanagan J., 1994, ApJS, 92, 53
- Wu, J., Vanden Berk, D. E., Brandt, W. N., et al. 2009, ApJ, 702, 767
- Wu, J., Brandt, W. N., Hall, P. B., et al. 2011, ApJ, 736, 28
- York, D. G., Adelman, J., Anderson, J. E., Jr., et al. 2000, AJ, 120, 1579
- Zoghbi, A., Fabian, A. C., Uttley, P., et al. 2010, MNRAS, 401, 2419
- Zoghbi, A., Uttley, P., & Fabian, A. C. 2011, MNRAS, 412, 59
- Zoghbi, A., & Fabian, A. C. 2011, MNRAS, 418, 2642

Table 1. PHL 1092 X-ray observations, X-ray/UV flux densities, and UV/optical to X-ray spectral indices. T_{exp} is in units of ks and refers to the net exposure in the EPIC-pn detector after filtering for background periods. All observations were performed in the *XMM-Newton* EPIC Full Window (FW) observing mode except XMM(3), for which the Large Window (LW) mode was used. For XMM(1) no spectral information is however available and the flux has been determined from the EPIC-pn light curve. The 2 keV flux density $f_{2\text{keV}}$ is given in units of $10^{-32} \text{ erg s}^{-1} \text{ cm}^{-2} \text{ Hz}^{-1}$, and the UV/optical ones in units of $10^{-27} \text{ erg s}^{-1} \text{ cm}^{-2} \text{ Hz}^{-1}$. The typical uncertainty on flux densities is 4–5 per cent at most (e.g. W2 filter). The rest-frame 2500 Å flux density is extrapolated from the nearest available OM filter using a spectral index of $\alpha_{\nu} = -0.70$ (Wu et al. 2001). $\Delta\alpha_{\text{ox}}$ is the difference between the observed value and that expected from the 2500 Å luminosity using the well known anti-correlation between α_{ox} and L_{2500} ($\alpha_{\text{ox}}^{\text{expected}} = -1.48$ for PHL 1092). The rest-frame effective wavelength of the OM filters are: 1519 Å (W2); 1655 Å (M2); 2084.5 Å (W1); 2464 Å (U).

| XMM-Newton observations and optical/UV/X-ray properties | | | | | | | | | | | | |
|---|------------|------------------|-----------|-------------------|-----------------|-----------------|-----------------|----------------|------------|-----------------------|----------------------|----------------------------|
| Obs. | Date | T_{exp} | Obs. mode | $f_{2\text{keV}}$ | f_{W2} | f_{M2} | f_{W1} | f_{U} | f_{2500} | α_{W2x} | α_{ox} | $\Delta\alpha_{\text{ox}}$ |
| XMM(1)* | 2000-07-31 | 25 | FW | 10 | 2.81 | | | | 3.98 | -1.86 | -1.77 | -0.29 |
| XMM(2)* | 2003-07-18 | 23 | FW | 31 | 2.69 | | | | 3.81 | -1.65 | -1.57 | -0.09 |
| XMM(3)* | 2008-01-20 | 57 | LW | 0.12 | 2.94 | | | | 4.17 | -2.67 | -2.51 | -1.03 |
| XMM(4) | 2009-06-27 | 24 | FW | 0.51 | 2.52 | 3.02 | 3.23 | 3.32 | 3.35 | -2.38 | -2.23 | -0.75 |
| XMM(5) | 2010-07-07 | 22 | FW | 3.1 | 2.72 | 2.75 | 2.99 | | 3.40 | -2.07 | -1.93 | -0.45 |
| XMM(6) | 2010-12-30 | 25 | FW | 2.4 | 2.68 | 2.88 | 3.01 | 3.20 | 3.23 | -2.11 | -1.97 | -0.49 |

* For the first three observations, f_{2500} is obtained by extrapolating f_{W2} assuming a spectral index of $\alpha_{\nu} = -0.70$. However, as discussed in Section 4.1.1, the W2 filter is centred at 1519 Å which coincides with the wing of the broad, blueshifted, and possibly variable C IV emission line. Hence, f_{2500} is not highly reliable, which affects the derived values of α_{W2x} , α_{ox} , and $\Delta\alpha_{\text{ox}}$.

Table 2. Best-fitting parameters for the phenomenological model comprising Galactic absorption, a multi-coloured blackbody, and a power-law (with slope forced to be the same in all the *XMM-Newton* observations). The inner disc blackbody temperature is not redshift-corrected and is given in units of keV. Fluxes in the 0.5–2 keV and 2–10 keV band are in c.g.s. units.

| Phenomenological model | | | | | $\chi^2/\text{dof} = 425/357$ | |
|------------------------|------------------|---------------------|---------------|---------------------|-------------------------------|--|
| Obs. | kT_{in} | N_{diskbb} | Γ | $\log F_{0.5-2}$ | $\log F_{2-10}$ | |
| XMM(2) | 0.11 ± 0.01 | 1520 ± 187 | 2.0 ± 0.3 | -12.254 ± 0.007 | -12.76 ± 0.07 | |
| XMM(3) | 0.08 ± 0.03 | 504 ± 500 | – | -14.630 ± 0.094 | ≤ -14.20 | |
| XMM(4) | 0.11 ± 0.03 | 30 ± 25 | – | -14.088 ± 0.063 | ≤ -14.00 | |
| XMM(5) | 0.10 ± 0.02 | 1666 ± 298 | – | -12.902 ± 0.014 | -13.63 ± 0.10 | |
| XMM(6) | 0.10 ± 0.01 | 373 ± 93 | – | -13.190 ± 0.018 | -13.95 ± 0.10 | |

Table 3. Best-fitting parameters for the baseline model. Columns with only one entry refer to parameters that have been forced to be the same as in the previous row. We report results for both $a = 0$ and $a = 0.998$ as they are statistically equivalent. The black hole mass is in units of $10^8 M_{\odot}$. The outer corona radius R_{c} is in units of $r_g = GM_{\text{BH}}/c^2$ and the temperature of the electron population responsible for the soft X-ray excess (kT_{e}) is in units of keV. The best-fitting X-ray unabsorbed luminosity is also reported for reference in units of $10^{43} \text{ erg s}^{-1}$ in the soft 0.5–2 keV and hard 2–10 keV band for the $a = 0$ model (as they are of course identical for the $a = 0.998$ case). We do not report errors as these luminosities are mostly based upon model extrapolation.

| Baseline model ($a = 0$) | | | | | | | | | $\chi^2/\text{dof} = 480/370$ | |
|--------------------------------|-----------------|--------------------------|-----------------|-----------------|-------------------|---------------------|-----------------|-------------|-------------------------------|--|
| Obs. | M_{BH} | $\log(L/L_{\text{Edd}})$ | R_{c} | kT_{e} | τ_{e} | Γ_{h} | f_{pl} | $L_{0.5-2}$ | L_{2-10} | |
| XMM(2) | 2.37 ± 0.25 | 0.39 ± 0.08 | 9.80 ± 0.70 | 0.12 ± 0.01 | 42 ± 16 | 2.8 ± 0.2 | 0.29 ± 0.11 | 65.0 | 5.88 | |
| XMM(3) | – | – | 6.39 ± 0.08 | – | – | – | 0.55 ± 0.15 | 0.29 | 0.04 | |
| XMM(4) | – | – | 6.61 ± 0.08 | – | – | – | 0.45 ± 0.15 | 0.98 | 0.11 | |
| XMM(5) | – | – | 8.06 ± 0.32 | – | – | 2.1 ± 0.3 | 0.05 ± 0.04 | 19.0 | 0.77 | |
| XMM(6) | – | – | 7.48 ± 0.20 | – | – | – | 0.06 ± 0.04 | 8.77 | 0.57 | |
| Baseline model ($a = 0.998$) | | | | | | | | | $\chi^2/\text{dof} = 480/370$ | |
| XMM(2) | 17.0 ± 2.0 | -0.51 ± 0.08 | 1.60 ± 0.06 | 0.12 ± 0.01 | 42 ± 15 | 2.8 ± 0.2 | 0.30 ± 0.11 | – | – | |
| XMM(3) | – | – | 1.27 ± 0.01 | – | – | – | 0.56 ± 0.13 | – | – | |
| XMM(4) | – | – | 1.29 ± 0.01 | – | – | – | 0.43 ± 0.12 | – | – | |
| XMM(5) | – | – | 1.41 ± 0.04 | – | – | 2.1 ± 0.3 | 0.05 ± 0.04 | – | – | |
| XMM(6) | – | – | 1.36 ± 0.03 | – | – | – | 0.08 ± 0.05 | – | – | |

Table 4. Best-fitting parameters for the absorption model. The soft excess is modelled as Comptonization in an optically thick corona, and the intrinsic X-ray flux is assumed to be constant, i.e. one and the same in all the *XMM-Newton* observations. The coronal parameters are as follows: $kT_e = 0.19 \pm 0.2$ keV, $\tau = 15 \pm 8$, $\Gamma_h = 1.8 \pm 0.1$, $R_c = 15 \pm 5 r_g$, and $f_{pl} = 0.05 \pm 0.03$. All the above parameters are forced to be the same at all flux levels. The absorber column density is in units of 10^{22} cm^{-2} . Its ionisation state reaches the lower limit defined in the absorption model we use ($\log \xi = -3.0$), as indicated by the subscript p (“pegged”). The absorption line energy is in units of keV and is given in the observed-frame.

| Absorption model ($a = 0$) | | | | | | | $\chi^2/\text{dof} = 410/355$ |
|---|--------------------|-----------------------|-------------------|------------------|-----------------------|---------------------|--------------------------------------|
| $M_{\text{BH}} \equiv 2.37 \times 10^8 M_{\odot}$ | | | | | | | $\log(L/L_{\text{Edd}}) \equiv 0.39$ |
| Obs. | N_{H} | $\log \xi$ | C_f | E_{abs} | σ_{abs} | τ_{abs} | |
| XMM(2) | 100 _{fix} | $-3.0^{+2.0}_{-0.0p}$ | 0.190 ± 0.010 | 1.05 ± 0.03 | 0.20 ± 0.02 | 0.15 ± 0.03 | |
| XMM(3) | – | – | 0.996 ± 0.001 | – | – | ≤ 0.60 | |
| XMM(4) | – | – | 0.985 ± 0.005 | – | – | ≤ 0.60 | |
| XMM(5) | – | – | 0.725 ± 0.008 | – | – | 1.00 ± 0.10 | |
| XMM(6) | – | – | 0.884 ± 0.005 | – | – | 0.60 ± 0.10 | |

Table 5. Best-fitting parameters for the reflection-dominated model. The column density of the warm absorber (WA) is in units of 10^{22} cm^{-2} and the disc inclination i in degrees. F_{ref} is the total reflection flux over the whole band (here 0.001–300 keV) in units of $10^{-11} \text{ erg s}^{-1} \text{ cm}^{-2}$. Notice that F_{ref} is likely over-estimated (but in the same way in all observations) because of the unknown low-energy bound which should be set at the energy below which the efficiency of the Compton up-scattering of the soft UV/EUV disc photons producing the irradiating power law is negligible.

| Disc Reflection model ($a = 0.998$) | | | | | | | | | $\chi^2/\text{dof} = 420/353$ |
|---|------------------------------|--------------------------|---------------|------------|-------------------------|------------------|----------------------|-----------------|---------------------------------------|
| $M_{\text{BH}} \equiv 17.0 \times 10^8 M_{\odot}$ | | | | | | | | | $\log(L/L_{\text{Edd}}) \equiv -0.51$ |
| Obs. | $N_{\text{H}}^{(\text{WA})}$ | $\log \xi^{(\text{WA})}$ | q | i | $\log \xi_{\text{ref}}$ | F_{ref} | R_c | Γ_h | |
| XMM(2) | $0.05^{+0.03}_{-0.00p}$ | -2.1 ± 0.2 | 5.0 ± 0.3 | 53 ± 6 | 3.03 ± 0.04 | 9.2 ± 0.4 | 1.235 _{fix} | 2.57 ± 0.02 | |
| XMM(3) | – | $-3.0^{+0.1}_{-0.0p}$ | – | – | 1.93 ± 0.17 | 0.7 ± 0.3 | – | – | |
| XMM(4) | – | $-3.0^{+0.1}_{-0.0p}$ | – | – | 2.45 ± 0.14 | 2.6 ± 0.2 | – | 2.76 ± 0.03 | |
| XMM(5) | – | -2.5 ± 0.2 | – | – | 2.74 ± 0.10 | 4.5 ± 0.2 | – | – | |
| XMM(6) | – | -2.6 ± 0.2 | – | – | 2.58 ± 0.10 | 3.5 ± 0.2 | – | – | |